Vol. 29 No. 127 *Journal of the Ratio Research Laboratories* *July 1982*
Printed in Tokyo, Japan *pp. 53–102*

DEVELOPMENT OF REAL-TIME VLBI AND MEASUREMENTS OF SCINTILLATION

By
Nobuyuki KAWANO, Fujinobu TAKAHASHI, Taizo YOSHINO
Kunimasa KOIKE, Hiroshi KUMAGAI and Nobuhiro KAWAJIRI

(Received on January 20, 1982)

CONTENTS

ABSTRACT

An accurate real-time VLBI (Very Long Baseline Interferometry) system with 47 km baseline connected by a terrestrial microwave link was developped. Using the system three kinds of experiments as well as the measurement of phase stability were carried out.

The first is the determination of the difference in time of arrival (delay time) by the new method of the minimum redundant bandwidth synthesis and the multilevel fringe stopping. The second is the measurement of phase scintillations which occur along the path through the atmosphere. The phase scintillations were derived from the differences between the phase variations of the signals from CS (El = 47.8 deg.) and INTELSAT (El = 1.7 deg.). The last is the measurement of the visibility scintillations due to the solar wind by receiving radio waves from 3C273.

Introduction

The accuracy of the delay time measurement is inversely proportional to the receiving or recording bandwidth. Rogers[1] suggested sampling of several "frequency windows" and synthesizing phase of these windows in data analysis, which is called bandwidth synthesis. Provided that the frequency windows or channels are not too widely spaced and that some means are available to calibrate the instrumental phases for each window, it should be possible to extrapolate the phase from one channel to the next and hence to synthesize an apparent recording bandwidth equal to the largest separation of the channels.

The system reported in this paper is the second Japanese VLBI system (K−2)[2], which is connected by a terrestrial microwave link. The baseline length between two antennas is 47 km. In the K−2 system, the two new methods, "minimum redundant bandwidth synthesis"[3] and "multilevel fringe stopping in the time domain"[4], are adopted to make possible precise delay time and short-term phase scintillation measurements. Five 2 MHz channels can be switched sequentially. The selection of the channels is made in a cyclic fashion, synchronously altered at the both stations. The K-2 system has the potential for the delay-time and phase-measurement accuracies of 0.1 ns and 3 deg. respectively, as nearly the same as with the Mark III System of U.S.A.

Because of the potential for high capacity communications and the limitation of the integration time in VLBI, the tropospheric phase scintillations in microwave and millimeter wave regions are of considerable interest. Propagation effects resulting from atmospheric phenomena influence optimum utilization of these frequency regions and the minimum product of two antenna diameters in VLBI. However, the phase scintillation measurements have some difficulties, such as how to obtain the stabilized reference frequency signals. The problem was solved in a rather ingenious manner by Thompson *et al.*[5] They suggested the use of a stable master oscillator at the main station and a phase-locked remote oscillator at the remote station, and they demonstrated the measurements of amplitude and phase on a several tens km path over a water extending from near sea level [6], [7], [8]. Some phase scintillation measurements with a conventional interferometer were conducted on the path through the atmosphere [9], [10], [11]. The baselines for these measurements were shorter than 11.3 km, and hence they were too short to investigate the limitation of the integration time or the minimum product of two antenna diameters in VLBI. On the other hand, the phase scintillation measurement described in this thesis was made by VLBI system with the baseline of 47 km. The phase scintillation was derived from the difference between the phase variations of the signals from two satellites, one at rather high elevation angle and the other at a low elevation angle.

There is another cause for the limitation of the integration time in VLBI. That is the phase scintillations due to the solar wind. These scintillations were first measured with a coherent dual-frequency radio system on Mariner 10, and the observations at solar elongations of 11.5 deg. and 12.6 deg. showed that the density spectrum in the frequency range of $10^{-4} < f < 5 \times 10^{-1}$ Hz approximately fitted in power law[12]. The VLBI observations were carried out by Knight *et al*[13] on the baseline more than one thousand km. In this thesis, the visibility scintillations produced by phase variations due to the solar wind are reported. The visibility scintillations were measured on considerably short baseline, 47 km, for two weeks when the propagation path of radio waves from QSO 3C273 approached the sun.

1. Theoretical consideration on data reduction

1.1 Maximum-likelihood estimates of observables

The maximum-likelihood (ML) estimates of delay, delay rate and fringe phase were first applied by Rogers[1] and somewhat were expanded by Whitney[14]. Here, we review those calculations. For the purposes of this analysis, Whitney proposed the two receiver system as diagrammed in Fig. 1-1. The signal $\vec{S}$ is Gaussian noise and is represented by N complex components,

$$\vec{S} = (S_1, \ldots, S_j, \ldots, S_N) \; ; 1 < j < N \quad \ldots\ldots\ldots\ldots\ldots\ldots\ldots\ldots\ldots\ldots (1.1)$$

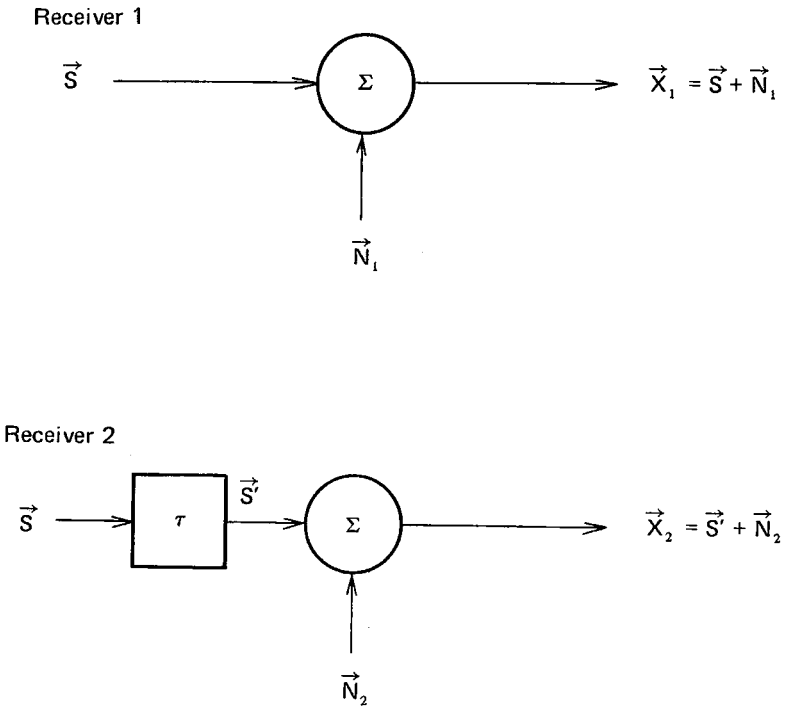

Fig. 1-1 Receiver models for maximum-likelihood estimate analysis.

for which each complex component has independent Gaussian real and imaginary parts. In the second receiver the signal $\vec{S}$ suffers a delay so that $\vec{S}'$ is related to $\vec{S}$ by the expression

$$\vec{S}' = \vec{S} \exp(-i\omega\tau) \quad \ldots\ldots\ldots\ldots\ldots\ldots\ldots\ldots\ldots\ldots\ldots\ldots\ldots\ldots\ldots\ldots (1.2)$$

where ω is a frequency in the observed spectrum.

At each station the signals are corrupted by additive independent Gaussian noises $\vec{N}_1$ and $\vec{N}_2$. The observed quantities $\vec{X}_1$ and $\vec{X}_2$ are then

$$\vec{X}_1 = \vec{S} + \vec{N}_1 \quad \ldots\ldots\ldots\ldots\ldots\ldots\ldots\ldots\ldots\ldots\ldots\ldots\ldots\ldots\ldots\ldots (1.3)$$

$$\vec{X}_2 = \vec{S}' + \vec{N}_2. \quad \cdots\cdots (1.4)$$

The ML estimates of τ, which we shall denote as $\hat{\tau}$, is defined as the value of $\tilde{\tau}$ which maximizes the conditional probability $p(\vec{X}_1, \vec{X}_2 | \tilde{\tau})$, where $\tilde{\tau}$ is the parameter whose value is varied to maximize $p(\vec{X}_1, \vec{X}_2 | \tilde{\tau})$. $p(X_1, X_2 | \tilde{\tau})$ is given by

$$p(X_1, X_2 | \tilde{\tau}) = \prod_{j=1}^{N} [\sigma_j^2 / (2\pi)^2 \cdot \sigma_{sj}^2 \cdot \sigma_{n1j}^2 \cdot \sigma_{n2j}^2$$

$$\cdot \exp(-|X_{1j}|^2/2\sigma_{n1j}^2 - |X_{2j}|^2/2\sigma_{n2j}^2 + |Y_j|^2/2\sigma_j^2) \quad \cdots\cdots (1.5)$$

where σ_j^2 and $|Y_j|^2$ are given by the expressions,

$$\sigma_j^2 = \sigma_{sj}^2 \cdot \sigma_{n1j}^2 \cdot \sigma_{n2j}^2 / (\sigma_{n1j}^2 \cdot \sigma_{n2j}^2 + \sigma_{sj}^2 \cdot \sigma_{n1j}^2$$

$$+ \sigma_{sj}^2 \cdot \sigma_{n2j}^2) \quad \cdots\cdots (1.6)$$

$$|Y_j|^2 = \sigma_j^4 \cdot |X_{1j}|^2 / \sigma_{n1j}^4 + \sigma_j^4 \cdot |X_{2j}^* \cdot \exp(-i\omega_j \tilde{\tau})|^2 / \sigma_{n2j}^4$$

$$+ 2\sigma_j^4 \cdot \mathrm{Re}[x_{1j} \cdot \dot{X}_{2j}^* \cdot \exp(-i\omega_j \tilde{\tau})] / \sigma_{n1j}^2 \cdot \sigma_{n2j}^2 \quad \cdots\cdots (1.7)$$

and σ_{sj}^2, σ_{n1j}^2, σ_{n2j}^2 denote the variances of $\vec{S}$, $\vec{N}_1$, $\vec{N}_2$. Of the terms in the exponent of Equation (1.7) the last is a function of $\tilde{\tau}$. But $|X_{2j}^* \cdot \exp(-i\omega_j \tilde{\tau})|$ is equal to $|X_{2j}|$, so that to find the ML estimate of τ, it is sufficient to maximize

$$\sum_{j=1} \mathrm{Re}[X_{1j} \cdot X_{2j}^* \cdot \exp(-i\omega_j \tilde{\tau})] . \quad \cdots\cdots (1.8)$$

This is just cross-correlation with fringe rotation followed by summation over independent points in the frequency spectrum. This analysis can easily be extended to find the ML estimate of fringe phase ϕ, that is

$$\mathrm{Max}[\mathrm{Re}\{\sum_{j=1} X_{1j} \cdot X_{2j}^* \exp(-i\omega_j \tilde{\tau} - i\tilde{\phi})\}] . \quad \cdots\cdots (1.9)$$

This analysis is extended to estimate the delay rate $\dot{\tau}$. For the case where $|\dot{\tau}| \ll 1$, an observation may be broken into many time-segments such that the change of delay during each segment t_k is small. The expression (1.9) may be evaluated for each of these segments after $\tau \to \tau + \dot{\tau} t_k$

$$\mathrm{Max}[\sum_{k=1}^{K} \sum_{j=1}^{J} \mathrm{Re}\{X_{1j} \cdot X_{2j}^* \exp[-i\{\omega_j(\tilde{\tau} + \tilde{\dot{\tau}} t_k) + \tilde{\phi}\}]\}] \quad \cdots\cdots (1.10)$$

where $\tilde{\tau}$, $\tilde{\dot{\tau}}$ and $\tilde{\phi}$ are the "trial parameters" and X_{1j} and X_{2j} are functions of k. The fringe phase estimate $\hat{\phi}$ is found in a similar manner by the expression

$$\tan(\hat{\phi}) = \mathrm{Im}\left[\sum_{k=1}^{K}\sum_{j=1}^{J} X_{1j}\cdot X_{2j}^{*}\cdot\exp\left\{-i\omega_j(\hat{\tau}+\dot{\hat{\tau}}\,t_k)\right\}\right] /$$

$$\mathrm{Re}\left[\sum_{k=1}^{K}\sum_{j=1}^{J} X_{1j}\cdot X_{2j}^{*}\cdot\exp\left\{i\omega_j(\hat{\tau}+\dot{\hat{\tau}}\,t_k)\right\}\right] \quad \ldots\ldots\ldots\ldots (1.11)$$

where $\hat{\tau}$ and $\dot{\hat{\tau}}$ denote ML estimates in the delay and delay rate.

1.2 Cross-spectral function

It is impossible for the current electronics to directly obtain X_{1j} and X_{2j} in Equation (1.10) through the Fourier transform of the video signals of several MHz. Therefore, the video signals are cross-correlated in the time domain by a correlator and reduced by integrating the cross-correlation functions. The Fourier transform of the integrated cross-correlation function gives $X_{1j}\cdot X_{2j}^{*}$ in Equation (1.10). This analysis under the ideal condition was discussed by Rogers[1] and many other researchers[14], [15], [16], [17]. Here, we describe the practical application of their analyses.

The signal y(t) at the remote antenna is a delayed replica of signal x(t) at the reference antenna, and

$$y(t) = x(t-\tau_g) \quad \ldots\ldots\ldots\ldots (1.12)$$

and the double-sided Fourier transform of y(t) is

$$y(\omega) = x(\omega)\cdot\exp(-i\omega\tau_o)\,. \quad \ldots\ldots\ldots\ldots (1.13)$$

we mix the reference signal of an angular frequency ω_X and phase ϕ_X with x(t) in the remote signal of ω_Y, ϕ_Y and select the upper sideband, and the frequency domain descriptions of signals are

$$X(\omega) = x(\omega+\omega_x)\cdot\exp(-i\phi_x) \quad \ldots\ldots\ldots\ldots (1.14)$$

$$Y(\omega) = y(\omega+\omega_y)\cdot\exp(-i\phi_y)\,. \quad \ldots\ldots\ldots\ldots (1.15)$$

The cross-spectral function $S'_{xy}(\omega)$ is

$$S'_{xy}(\omega) = X(\omega)\cdot Y^{*}(\omega)$$

$$= S_{xx}(\omega+\omega_x)\cdot\exp(i\Phi') \quad \ldots\ldots\ldots\ldots (1.16)$$

where Φ' is given by the expression

$$\Phi' = (\omega+\omega_x)\cdot\tau_o + (\phi_y-\phi_x) + (\omega_y-\omega_x)\cdot t\,. \quad \ldots\ldots\ldots\ldots (1.17)$$

Considering frequency-phase and frequency-amplitude characteristics, we obtain

$$S'_{xy}(\omega) = \overline{S_{xx}}\cdot|G_{xy}(\omega+\omega_o)|\cdot\exp[i\Psi_{xy}(\omega+\omega_o)]\cdot\exp(i\Phi') \quad \ldots\ldots\ldots (1.18)$$

where $\overline{S_{xx}}$, $G_{xy}(\omega+\omega_o)$ and $\psi_{xy}(\omega+\omega_o)$ denote the amplitude of x(t), frequency-ampli-

tude and frequency-phase characteristics of receivers respectively. We can devide ψ_{xy} $(\omega + \omega_o)$ into two parts

$$\Psi_{xy}(\omega + \omega_o) = (\omega + \omega_o) \cdot \tau_i + \Delta\Psi_{xy}(\omega) \quad \ldots\ldots (1.19)$$

The first term in Equation (1.19) shows the instrumental delay and the second is the inherent frequency-phase characteristic. τ_o consists of the geometrical delay time τ_g, the propagation delay time τ_p and the time synchronization error τ_e. Then, Equations (1.16) and (1.17) can be rewritten by

$$S_{xy}(\omega) = \overline{S_{xx}} \cdot |G_{xy}(\omega + \omega_o)| \cdot \exp(i\Phi) \quad \ldots\ldots (1.20)$$

and

$$\Phi = (\omega + \omega_o) \cdot (\tau_g + \tau_p + \tau_e + \tau_i) + (\phi_y - \phi_x) + (\omega_y - \omega_x) \cdot t + \Delta\Psi_{xy}(\omega) \quad \ldots\ldots (1.21)$$

It is our purpose to estimate τ_g, τ_p, τ_e and $\omega_y - \omega_x$ with high accuracy, so that Equation (1.20) is one of the most fundamental equation in VLBI.

1.3 Cross-correlation function and fringe stopping

A cross-correlation function is defined as

$$R_{xy}(\tau) = \int x(t) \cdot y(t + \tau)\, dt \quad \ldots\ldots (1.23)$$

A cross-correlation function $R_{xy}(\tau)$ is related to a cross-spectral function $S_{xy}(\omega)$ by

$$R_{xy}(\tau) = \mathrm{IFT}\,[S_{xy}(\omega)] \quad \ldots\ldots (1.24)$$

In opposition, a cross-correlation function is given by

$$S_{xy}(\omega) = \mathrm{FT}\,[R_{xy}(\tau)] \quad \ldots\ldots (1.25)$$

where FT and IFT express Fourier transform and inverse Fourier transform respectively. Assuming that $G_{xy}(\omega)$ in Equation (1.20) which is the expression of $G_{xy}(\omega + \omega_o)$ in the video frequency domain, is constant with respect to ω over the bandwidth, the following expressions are obtained

$$S_{xy}(\omega) = G_{xy}(\omega) \cdot \exp(i\Phi) \quad \ldots\ldots (1.26)$$

$$R_{xy}(\tau) = 2 \cdot B \cdot \cos[\theta + \omega_o(\tau_g + \tau_p + \tau_e + \tau_i) + \pi B\tau'] \cdot [\sin(\pi B\tau')/\pi B\tau'] \quad \ldots\ldots (1.27)$$

where θ, τ', and $G_{xy}(\omega)$ are

$$\Phi = (\omega + \omega_o) \cdot (\tau_g + \tau_p + \tau_e + \tau_i) + \Delta\psi_{xy}(\omega)$$

$$\theta = (\phi_y - \phi_x) + (\omega_y - \omega_x) \cdot t + \Delta\psi_{xy} \quad \cdots\cdots (1.28)$$

$$\tau' = \tau + \tau_g + \tau_p + \tau_e + \tau_i \quad \cdots\cdots (1.29)$$

$$G_{xy}(\omega) = 1/S_{xx} \quad \cdots\cdots (1.30)$$

We note that the long period integration of $R_{xy}(\tau)$ or $S_{xy}(\omega)$ diminishes the correlation when the geometrical delay varies in time, even if the changes τ_p, τ_e, and τ_i during the period are small. For this reason, the fringe stopping which compensates the change of the fringe phase Φ is indispensable for the case of long period integration. Fig. 1-2 shows the samples cross-correlation function in case when the phase φ's, which are the arguments of $R_{xy}(\tau)$, are 0, 90, 180 and 270 deg.

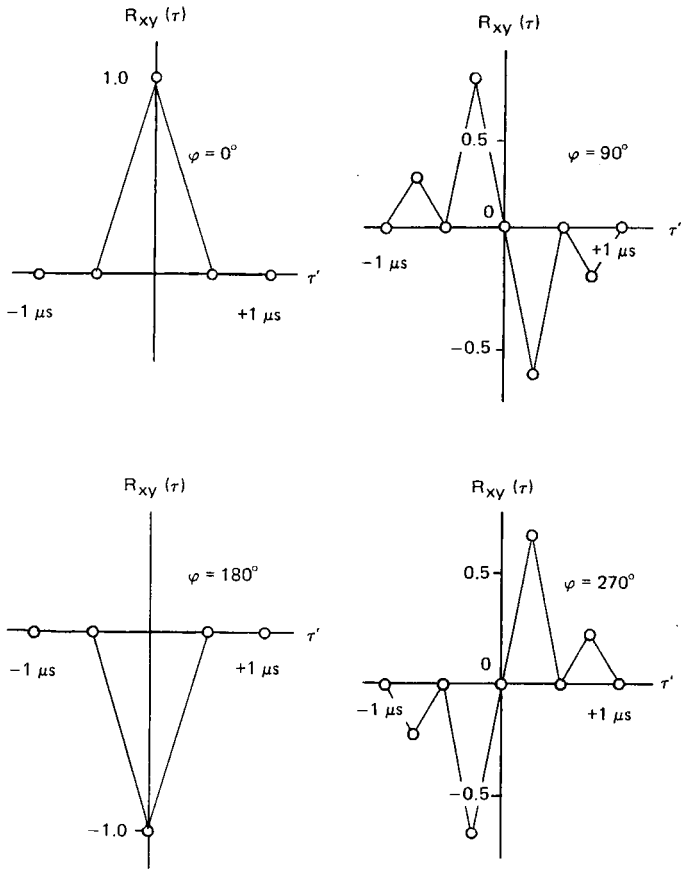

Fig. 1-2 Cross-correlation functions in the phase differences of 0°, 90°, 180° and 270°.

The video signals x(t) and y(t) at the two stations are given by

$$x(t) = \int X(\omega) \cdot \exp(i\omega t) \cdot d\omega \quad \ldots\ldots (1.31)$$

$$y(t) = \int X(\omega) \cdot \exp(-i\Phi) \cdot \exp(i\omega t) \cdot d\omega . \quad \ldots\ldots (1.32)$$

The cross-correlation function has the form

$$R_{xy}(\tau) = \int [\int X(\omega) \cdot \exp(i\omega t) \cdot d\omega] \cdot [\int X(\omega') \exp\{i\omega'(t+\tau)\} \cdot \exp(i\Phi) \cdot d\omega'] * \cdot dt . \quad \ldots\ldots (1.33)$$

The integration time is chosen short enough, $\omega\tau_g$ can be taken as a constant, and only $\omega_o \tau_g$ changes the phase for the integration time. The fringe rate is given approximately by

$$F_r = \omega_o \dot{\tau}_g \quad \ldots\ldots (1.34)$$

and we can also rewrite Φ by the expression

$$\Phi = F_r \cdot t + \theta_o . \quad \ldots\ldots (1.35)$$

Considering Equation (1.35), we can rewrite Equation (1.33)

$$\begin{aligned} R_{xy}(\tau) &= \int [\int X(\omega) \cdot \exp(i\omega t) \cdot d\omega] \cdot \exp\{i(F_r \cdot t + \theta_o)\} \\ &\quad \cdot [\int X(\omega') \cdot \exp\{i\omega'(t+\tau)\} \cdot d\omega'] * \cdot dt \\ &= \int x(t) \cdot \exp\{i(F_r \cdot t + \theta_o)\} \cdot x(t+\tau) \cdot dt . \quad \ldots\ldots (1.36) \end{aligned}$$

For the purpose of the fringe stopping, the trial function $\exp[-i(F_r' \cdot t + \theta_o')]$, which includes a guess for the unknown term, is multiplied by Equation (1.36)

$$\begin{aligned} R'_{xy}(\tau) &= \int x(t) \cdot \exp[i(F_r \cdot t + \theta_o)] \\ &\quad \cdot \exp[-i(F'_r \cdot t + \theta'_o)] \cdot x(t+\tau) \cdot dt . \quad \ldots\ldots (1.37) \end{aligned}$$

When the trial function is equal to $F_r \cdot t + \theta_o$, $R_{xy}(\tau)$ becomes an auto-correlation function $R_{xx}(\tau)$. It is clear that $R_{xy}(\tau)$ is maximized when $F'_r \cdot t + \theta'_o$ is equal to $F_r \cdot t + \theta_o$ because the integrated product of two sinusoidal functions are nonvanishing only when the trial function and the actual value are equal. In practice, F'_r is evaluated with high accuracy, from the earth rotation, antenna positions, star positions, etc., and the following calculation is conducted

$$R'_{xy}(\tau) = \int x(t) \cdot \exp[i(F_r \cdot t + \theta_o)] \cdot \exp(-iF'_r \cdot t)\, x(t+\tau) \cdot dt . \quad \ldots\ldots (1.38)$$

When F'_r is close to F_r, $R_{xy}(\tau)$ is approximately

$$R_{xy}(\tau) = R_{xx}(\tau) \exp\left[i\left(\langle \Delta F_r \cdot t \rangle + \theta_o\right)\right] \quad \ldots\ldots\ldots\ldots\ldots\ldots\ldots\ldots\ldots\ldots (1.39)$$

where $\langle \Delta F_r \cdot t \rangle$ denotes the mean of the $(F'_r - F_r) \cdot t$. Equation (1.39) shows that the cross-correlation is nonvanishing if the integration time is chosen short enough and $\Delta F_r \cdot t$ is nearly zero. Although the calculation of Equation (1.39), which is called "coarse fringe stopping", is performed with a correlator, "fine fringe stopping" for the residual fringe rate $\Delta F_r \cdot t$ is usually evaluated with a host computer by the method of the ML estimate. We note that outputs from a correlator are complex cross-correlation functions instead of real cross-correlation functions.

The video signals are clipped, sampled at the Nyquist frequency of 4 MHz in our system, and quantized to one bit. For each signal, the "a priori" value assumed for the delay time and quantized in unit of the sample period (250 ns), is kept constant. This value m is termed "bit offset" between the two data streams. Then we can rewrite Equation (1.38) by

$$R_{xy}(\ell) = \left(\frac{\beta}{N}\right) \sum_{n=1}^{N} x(n) \cdot \cos(F_r' \cdot t) \cdot y(n + m + \ell)$$

$$- i\left(\frac{\beta}{N}\right) \sum_{n=1}^{N} x(n) \cdot \sin(F_r' \cdot t) \cdot y(n + m + \ell) \quad \ldots\ldots\ldots\ldots\ldots (1.40)$$

$$\ell = -L, -L-1, \ldots, -1, 0, 1, \ldots, L-1 \quad \ldots\ldots\ldots\ldots\ldots\ldots\ldots\ldots\ldots (1.41)$$

where n is the sample index within the integration time. N is number of samples or bits for the inteval of each stream. ℓ is the integer index for the offsets in the evaluation of the correlation function, so called "lag". The calculations in Equation (1.40) must be performed every 250 ns, but this speed of the calculation is too fast for the present hardware or computer. Whitney *et al.* proposed three-level approximation to sine and cosine function, as shown in Fig. 1-3. This three-level representation is especially efficient to use since multipli-

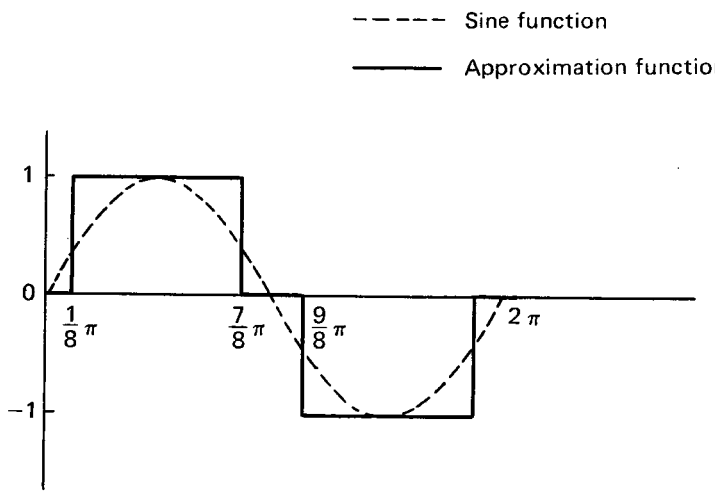

Fig. 1-3 Approximation function with 3 levels for fringe stopping.

cation by minus one is accomplished only by changing the sign of the data sample and multiplication by zero is accomplished just by omitting the term in the summation process. These multiplications can be performed only by use of simple devices.

1.4 Multi-level fringe stopping in the time domain

The approximation mentioned above is so rough that the coherence decreases since the summation is omitted when the approximation function is zero, and the term omitted is a quarter of the whole term. Furthermore, this approximation makes an error in the short-term phase difference estimation in the case when only a few periods of the sinusoidal function are included in the whole integration interval. Kawano[4] proposed "multi-level fringe stopping in the time domain" which can be performed by use of EX-NOR devices and counters.

Fig. 1-4 shows a five-level approximation to sine function. Assuming that the approximation function is taken as a constant for the interval $n_i \sim n_{i+1}$, we obtain

$$R_{xy}(\ell) = r'_c(\ell) - ir'_s(\ell) \quad \cdots\cdots (1.42)$$

$$r'_c(\ell) = \left(\frac{\beta}{MN}\right) \sum_{n=1}^{N} x(n) \cdot y(n+m+\ell) \cdot \{I\} \quad \cdots\cdots (1.43)$$

$$r'_s(\ell) = \left(\frac{\beta}{MN}\right) \sum_{n=1}^{N} x(n) \cdot y(n+m+\ell) \cdot \{J\} \quad \cdots\cdots (1.44)$$

where the factor β accounts for the average reduction in the correlation caused by the approximations to sine and cosine functions, and $\{I\}$, $\{J\}$ denote the multi-level approximations to cosine and sine functions respectively. M is (the number of level $-$ 1)/2. For example, in the case of the five-level approximation, $\{I\}$ and $\{J\}$ are given by

$$\{I\}, \{J\} = \begin{array}{rl} 2, 0 & ; n = 1 \sim n_1 \\ 1, 1 & ; n = n_1 + 1 \sim n_2 \\ 0, 2 & ; n = n_2 + 1 \sim n_3 \\ -1, 1 & ; n = n_3 + 1 \sim n_4 \\ -2, 0 & ; n = n_4 + 1 \sim n_5 \\ -1, -1 & ; n = n_5 + 1 \sim n_6 \\ 0, -2 & ; n = n_6 + 1 \sim n_7 \\ 1, -1 & ; n = n_7 + 1 \sim n_8 \\ \cdot\ \cdot & \cdot \\ \cdot\ \cdot & \cdot \end{array} \quad \cdots\cdots (1.45)$$

The calculation in Equations (1.43) and (1.44) are performed by use of up-down counters and EX-NOR devices since multiplication by minus two is accomplished by subtracting two from the sum of the correlation, and multiplication by two is accomplished by adding two to the sum. The so-called cosine and sine parts of the complex correlation function, $r_c(\ell)$

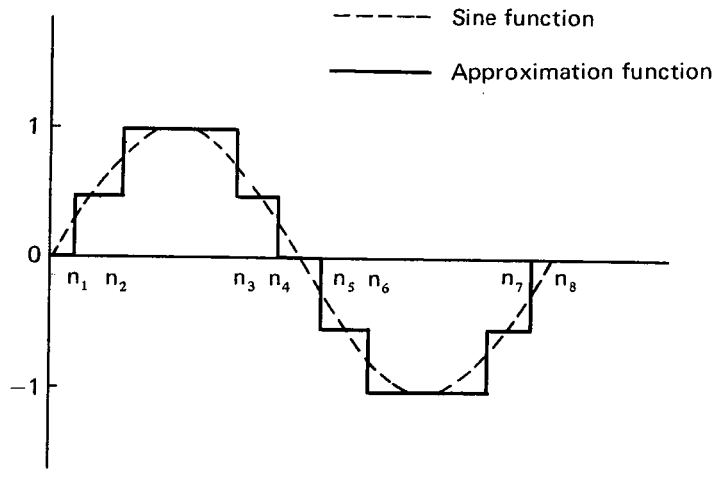

Fig. 1-4 Approximation function with 5 levels for fringe stopping.

and $r_s(\ell)$, respectively are thus approximated by

$$r_c(\ell) = \sin\left[\frac{\pi}{2} r'_c(\ell)\right]$$

$$r_s(\ell) = \sin\left[\frac{\pi}{2} r'_s(\ell)\right] \quad \cdots\cdots (1.46)$$

where the familiar Van Vleck clipping correction[18] has been applied to the corresponding parts of the correlation functions $r'_c(\ell)$ and $r'_s(\ell)$ of the clipped signal. The complex correlation function corresponding to $R_{xy}(\ell)$ is given by

$$R_{xy}(\ell) = r_c(\ell) - i r_s(\ell) . \quad \cdots\cdots (1.47)$$

The complex correlation function is transformed to the frequency domain. The cross-spectral function is given by

$$S_{xy}(k) = \sum_{\ell=-L}^{L-1} R_{xy}(\ell) \cdot \exp\left[-i\pi\ell k/L\right] . \quad \cdots\cdots (1.48)$$

$S_{xy}(k)$ corresponds to the kth frequency component of the video signal. We note that the delay time and fringe rate has been subtracted by the shifted bits and F'_r, by the method of the bit offset and the coarse fringe stopping, so that $S_{xy}(k)$ corresponds to

$$S_{xy}(\omega) = G_{xx}(\omega) \exp\left[i(\omega + \omega_o)(\tau_o - m\cdot\Delta\tau_b) + \langle \Delta F_r \cdot t \rangle + \theta_o\right] \quad \cdots\cdots (1.49)$$

and $\Phi(\omega)$ is

$$\Phi(\omega) = (\omega + \omega_o)\cdot\Delta\tau + \langle \Delta F_r \cdot t \rangle + \theta_o \quad \cdots\cdots (1.50)$$

where $\Delta\tau_b$ denotes the sample interval. $\Delta\tau$ (= τ_o - m · $\Delta\tau_b$) and ΔF_r are called a residual delay and residual fringe rate. $S_{xy}(k)$ can be obtained every interval of the integration, so that the ML estimate of the residual delay and the residual fringe rate is given by

$$\underset{j}{\text{Max}} \sum_{k} \sum [\text{Re} \left\{ S^{j}_{xy}(k) \cdot \exp [-i \left\{ (\omega + \omega_o) \cdot \Delta\tau + \right.\right.$$

$$\left.\left. \Delta F_r \cdot t + \theta \right\}] \right\}] \quad \ldots\ldots\ldots\ldots\ldots\ldots\ldots\ldots\ldots\ldots\ldots\ldots (1.51)$$

where $\Delta\tau$ is the residual delay time and $S^{j}_{xy}(k)$ denotes a cross-spectral function for the jth interval.

1.5 Minimum redundant bandwidth synthesis

The bandwidth of a channel is limited to several MHz and the delay time measurement accuracy in one channel is of the order of a few hundred nanoseconds. Rogers[1] introduced reception of radio signals at several frequency windows or channels, and each bandwidth of them is several MHz. The phases of these channels are synthesized. Assuming that the frequency-phase and frequency-amplitude characteristics in Equation (1.20) have been corrected, the cross-spectral function of the kth channel is given by

$$S^{k}_{xy,j}(\omega) = \overline{S_{xx}} \cdot \exp [(\omega + \omega^{k}_{o}) (\tau_g + \tau_p + \tau_e) + \theta_k] . \quad \ldots\ldots\ldots\ldots\ldots (1.52)$$

θ_k is the phase difference between channels and the differences are independent of each other. θ_k is given by

$$\theta_k = (\omega + \omega^{k}_{o}) \cdot \tau_i + (\omega^{k}_{y} - \omega^{k}_{x}) \cdot t_j + (\phi^{k}_{y} - \phi^{k}_{x})$$

$$\sim \omega^{k}_{o} \cdot \tau_i + (\omega^{k}_{y} - \omega^{k}_{x}) \cdot t_j + (\phi^{k}_{y} - \phi^{k}_{x}) . \quad \ldots\ldots\ldots\ldots\ldots\ldots\ldots (1.53)$$

Assuming that θ_k have been calibrated, the ML estimate for the bandwidth synthesis is given by

$$\underset{j}{\text{Max}} \sum_{k} \sum \text{Re} [S^{k}_{xy,j}(\omega) \cdot \exp \left\{ -i [(\omega + \omega^{k}_{o}) \cdot \tau + \right.$$

$$\left. F_r \cdot t_j + \theta_k] \right\}] \quad \ldots\ldots\ldots\ldots\ldots\ldots\ldots\ldots\ldots\ldots\ldots (1.54)$$

Now, we describe the problem, how to allocate the frequency windows or channels. The cross-spectral function for the sum of channels is given by

$$S(\omega) = \sum_{k} \overline{S_{xx}} (\omega^{k}_{o} + \omega) \cdot \exp (i\theta_k) \cdot \exp [i\omega^{k}_{o} (\tau_g + \tau_p + \tau_e)]$$

$$\exp [i\omega (\tau_g + \tau_p + \tau_e)] . \quad \ldots\ldots\ldots\ldots\ldots\ldots\ldots\ldots\ldots (1.55)$$

On the analogy with Equation (1.27), the corresponding cross-correlation function is given by

$$R_{xy}(\tau) = 2 \cdot |D(\tau')| \cdot \cos [\omega_o (\tau_g + \tau_p + \tau_e) + \arg D(\tau')] \quad \ldots\ldots (1.56)$$

where $D(\tau')$ is given by

$$D(\tau') = \sum_k D_k(\tau') \quad \ldots\ldots (1.57)$$

and

$$D_k(\tau') = \exp [i(\omega_k \tau' + \theta_k)] \cdot [B_1(\tau') + iB_2(\tau')] \quad \ldots\ldots (1.58)$$

$$\omega_1 = 0 \sim \omega$$

$$\omega_2 = (\omega_o^2 - \omega_o^1) \sim (\omega_o^2 - \omega_o^1) + \omega$$

$$\omega_k = (\omega_o^k - \omega_o^1) \sim (\omega_o^k - \omega_o^1) + \omega$$

$$\tau' = \tau + \tau_g + \tau_p + \tau_e$$

$$B_1(\tau) = \int S_{xx}(\omega_k + \omega) \cdot \cos(\omega\tau) \cdot \frac{d\omega}{2\pi}$$

$$B_2(\tau) = \int S_{xx}(\omega_k + \omega) \cdot \sin(\omega\tau) \cdot \frac{d\omega}{2\pi}$$

Equation (1.56) indicates that the delay time measurement accuracy depends on $|D(\tau')|$. Assuming that a signal is filtered by receivers with a rectangular bandpass of width B Hz, $|D(\tau')|$ would become

$$|D(\tau')| = [B \cdot \sin(\pi B\tau')/\pi B\tau'] \cdot D_e(\tau') \quad \ldots\ldots (1.59)$$

where $D_e(\tau')$ is given by

$$D_e(\tau') = \left| \sum_k \exp(i\omega_o^k \tau') \right| \quad \ldots\ldots (1.60)$$

The magnitude of $D(\tau')$ is named the delay resolution function. Equation (1.59) is entirely analogous to the beam pattern of a linear-array antenna. According to the linear-array theory, the minimum redundant array of antennas[29] gives the highest possible resolution for a given aperture length. Kawaguchi and Kawano[3] suggested that the best frequency

configuration in the bandwidth synthesis is equivalent to the spacing of the minimum redundant array.

Assuming that any local signal is generated with the aid of a frequency multiplier, and the reference angular frequency is ω_s, the local angular frequency ω_o^k is given by

$$\omega_o^k = N_k \cdot \omega_s \quad \cdots\cdots (1.61)$$

where k = 0, 1, 2, 3, ... , K−1, and $N_o = 0$. We can rewrite equation (1.60) by the expression

$$D_e^2(\tau') = \left\{ 1 + \sum_{k=1}^{K-1} \exp\left[iN_k\omega_s\tau'\right] \right\} \cdot \left\{ 1 + \sum_{k=1}^{K-1} \exp\left[-iN_k\omega_s\tau'\right] \right\}$$

and the square of the delay resolution function is evaluated by[19]

$$D_e^2(\tau') = K + 2\sum_{k=1}^{M} \cos\left(N_j\omega_s\tau'\right) \quad \cdots\cdots (1.62)$$

where $M = {}_{k-1}C_2 + K-1$, and $\mathrm{Max}\left\{N_j\right\} = N_{max}$. N_{max} is the greatest multiple of the reference angular frequency ω_s. We can obtain the following five results from Equation (1.62).

1) $De(\tau')$ has the period of $2\pi/\omega_s$.
2) (Zero-redundancy)
   There are only four zero-redundant configurations.
   These are (0), (0, 1), (0, 1, 3), (0, 1, 4, 6).
3) (Minimum redundancy)
   Samples of the minimum redundant configurations are given in Table 1-1.
4) The sidelobe level decreases with the number of odd N_k.
5) The width of a peak in the delay resolution function is proportional to $1/(N_{max} \cdot \omega_s)$.

Fig. 1-5 shows the delay resolution function for the minimum redundant bandwidth synthesis which we adopted.

Table 1-1 Minimum redundant configurations

N	N_{max}	Configuration
5	9	0, 1, 4, 7, 9
6	13	0, 1, 6, 9, 11, 13
7	17	0, 1, 4, 10, 12, 15, 17
8	23	0, 1, 4, 10, 16, 18, 21, 29
9	29	0, 1, 4, 10, 16, 22, 24, 27, 29
10	36	0, 1, 3, 6, 13, 20, 27, 31, 35, 36
11	43	0, 1, 3, 6, 13, 20, 27, 34, 38, 42, 43

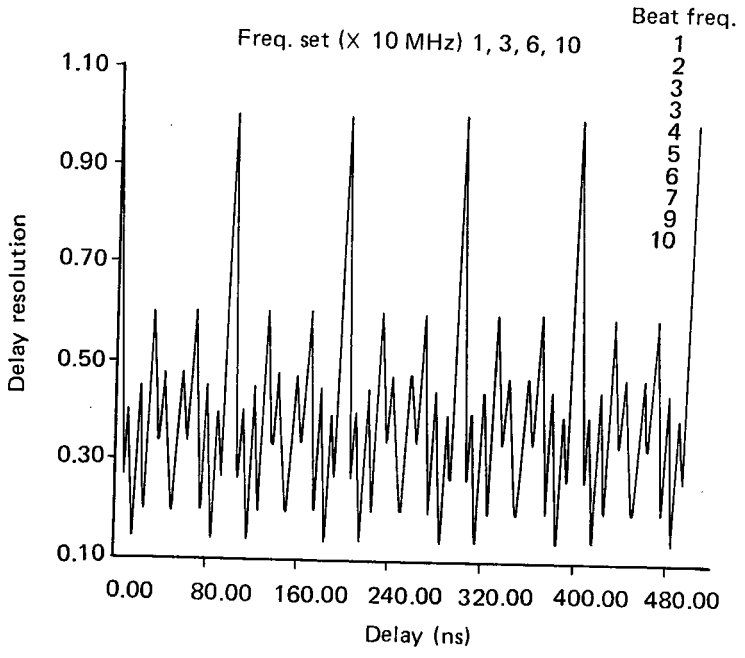

Fig. 1-5 Delay resolution function for the minimum redundant bandwidth synthesis of our system.

1.6 Sensitivity of delay time

The estimation error of delay time can be defined by the variance of σ^2_Φ. Assuming that T_{ax}, T_{ay}, T_{sx}, T_{sy} are the antenna noise temperatures due to radio sources and the system noise temperatures due mostly to receiver noises at the two stations, the variance σ^2_Φ in the common case where $T_{ax} \ll T_{sx}$ and $T_{ay} \ll T_{sy}$ is given by

$$\sigma^2_\Phi \sim T_{sx}T_{sy}/2BTT_{ax}T_{ay} \quad \cdots\cdots (1.63)$$

where B and T are the bandwidth and the integration time respectively. On the other hand, the signal-to-noise ratio which is equivalent to the coherence is well-known as

$$SNR = \sqrt{T_{ax} \quad T_{ay}/T_{sx} \quad T_{sy}}\ \sqrt{2 \cdot B \cdot T}\ . \quad \cdots\cdots (1.64)$$

From Equations (1.63) and (1.64) we obtain

$$\sigma_\Phi = 1/SNR\ . \quad \cdots\cdots (1.65)$$

An antenna noise temperature is a function of the antenna diameter, so that we can obtain SNR as a function of antenna diameters. Assuming that D_x and D_y are the diameters of the two antennas, Equation (1.64) becomes

$$SNR = 1/\sigma_\Phi = (\pi S_\circ \cdot D_x \cdot D_y/8k) \cdot (2\eta_x \cdot \eta_y \cdot B \cdot T/$$

$$T_{sx} \cdot T_{sy})^{1/2} \quad \cdots\cdots (1.66)$$

where S_o is the source flux density observed and η_x and η_y are the efficiencies of the two antennas. In the common case, an antenna efficiency is 0.4 ~ 0.7. k is the Boltzmann constant.

From the variance σ^2_Φ for one channel, given by Equation (1.63), we can easily evaluate the variance for the bandwidth synthesis. Equation (1.21) shows that the phase $\Phi(\omega)$ is directly proportional to a frequency, so that the delay is the slope of the phase versus frequency curve. The well-known variance of the slope is given by

$$\sigma_\tau = (1/\omega_s)\sqrt{K/(K\cdot \sum_{k=1}^{K-1} N_k^2 - \sum_{k=1}^{K-1} N_k \cdot \sum_{k=1}^{K-1} N_k}$$

$$\cdot \sqrt{K\cdot\sigma^2_\Phi/(K-2)}\,. \quad \cdots\cdots (1.67)$$

When the frequency configurations in the minimum redundant bandwidth synthesis are (0, 10, 40, 70, 90 MHz) and the variance for one channel is 0.1 radian, σ_τ reaches 0.08 ns in spite of about 2 ns for one channel. Thus, the bandwidth synthesis is really an effective method to the accurate delay time measurements.

1.7 Calculations of delay time and fringe rate

Fig. 1-6 shows a geometrical configuration of a pair of radio interferometer stations. Since these two antennas are separated by a distance D, there will be a difference in the

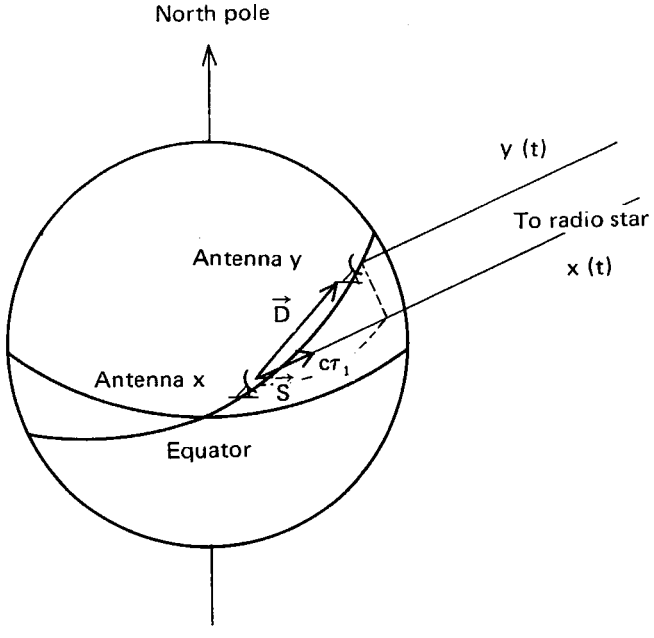

Fig. 1-6 Geometrical configuration in VLBI.

time of reception of the signal at the two antennas. This delay time τ_g is given by

$$\tau_g = (-1/c)\, \vec{D} \cdot \vec{S} \quad \ldots\ldots \quad (1.68)$$

where c is the speed of light, and $\vec{S}$ is a unit vector opposite to the direction of propagation of the wave front. Equation (1.68) is most usefully expanded in terms of the equatorial coordinate system of date. In this system, the right ascension and declination of the source are given by α_S and δ_S, while the equivalent quantities for the baseline vector $\vec{D}$ are α_B and δ_B. Explicitly writing out the dot product in Equation (1.68)

$$\tau_g = (-D/c) \left\{ \sin\delta_B \cdot \sin\delta_S + \cos\delta_B \cdot \cos\delta_S \cdot \cos(L_S - L_B) \right\} \quad \ldots\ldots \quad (1.69)$$

On the other hand, fringe rate F_r is defined by $\omega' \cdot \dot{\tau}_g$, where ω' is the received angular frequency. Then

$$F_r = -\omega' \cdot (D/c) \cdot \cos\delta_B \cdot \cos\delta_S \cdot \sin(L_S - L_B) \cdot (dL_B/dt)\,. \quad \ldots\ldots \quad (1.70)$$

Although the delay time and the fringe rate are the function of the earth rotation, general relativity, polar motion, earth tide, ocean loading, precession, nutation, etc., the prediction of the delay time and fringe rate for the bit-offset and the coarse fringe stopping in the correlator, does not need to consider these whole phenomena. The calculation accuracies desired are about one bit (250 ns) and several degrees for the integration period. If the baseline length and the received frequency are 1000 Km and 4 X 10^9 Hz respectively, the calculation accuracies required are given by

$$\sin\delta_B \cdot \sin\delta_S + \cos\delta_B \cdot \cos\delta_S \cdot \cos(L_S - L_B) < 7.5 \times 10^{-5} \quad \ldots\ldots \quad (1.71)$$

$$\cos\delta_B \cdot \cos\delta_S \cdot \sin(L_S - L_B) < 1.6 \times 10^{-5}\,. \quad \ldots\ldots \quad (1.72)$$

For these inequalities, the precession, nutation, polar motion and DUT1 are taken into consideration and SAO C-7 is adopted as a model of the earth, namely the adopted ellipsoid.

Each antenna position is conveniently expressed in terms of a right handed Cartesian coordinate system fastened to the earth with the x axis through Greenwich and the z axis along the instantaneous rotation axis. If the geodetic latitude is φ and the longitude is λ, the antenna position (X′, Y′, Z′), as shown in Fig. 1-7, is given by

$$\begin{pmatrix} X' \\ Y' \\ Z' \end{pmatrix} = \begin{pmatrix} (N + h) \cdot \cos(\varphi) \cdot \cos(\lambda) \\ (N + h) \cdot \cos(\varphi) \cdot \sin(\lambda) \\ (N \cdot P + h) \cdot \sin(\varphi) \end{pmatrix} \quad \ldots\ldots \quad (1.73)$$

where h is the height above the adopted ellipsoid, and

$$N = a/\sqrt{1 - e^2 \cdot \sin^2(\varphi)}$$

$$P = b^2/a^2\,.$$

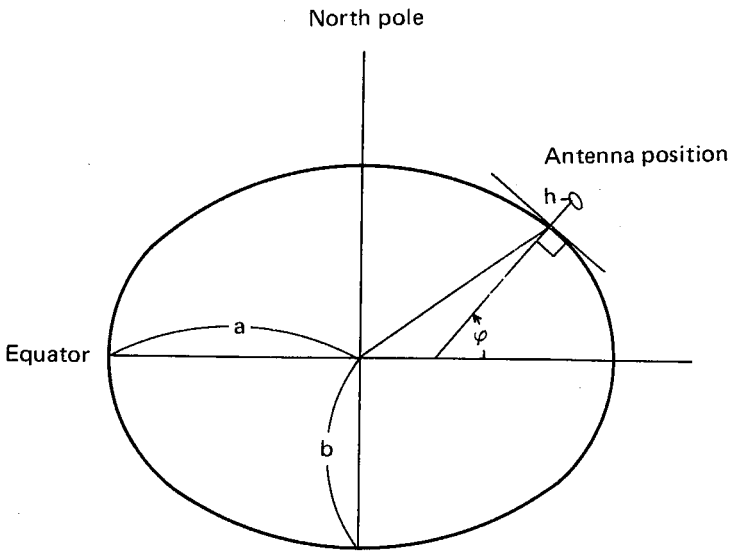

Fig. 1-7 Ellipsoid and antenna position.

a and b are the semimajor and semiminor axes of the adopted ellipsoid. The baseline vector $\vec{D}$ in terms of the earth fixed coordinate system is easily obtained by

$$\vec{D} = \begin{pmatrix} X'_y \\ Y'_y \\ Z'_y \end{pmatrix} - \begin{pmatrix} X'_x \\ Y'_x \\ Z'_x \end{pmatrix} \quad \cdots\cdots (1.74)$$

The baseline vector $\vec{D}$ in terms of true equatorial coordinates of date is given by

$$\vec{D}(t) = \mathbf{R} \cdot \mathbf{W} \cdot \vec{D} \quad \cdots\cdots (1.75)$$

where matrix **R** accounts for the earth's spin and the matrix **W** is for the polar motion. These are given by[20]

$$\mathbf{R} = \begin{pmatrix} \cos(\theta) & -\sin(\theta) & 0 \\ \sin(\theta) & \cos(\theta) & 0 \\ 0 & 0 & 1 \end{pmatrix}$$

where θ is the Greenwich apparent siderial time and

$$\mathbf{W} = \begin{pmatrix} 1 & 0 & -X_p \\ 0 & -1 & Y_p \\ X_p & Y_p & 1 \end{pmatrix}$$

where X_p is the component of geocentric angular position and Y_p is the corresponding angular component along the meridian 90° west of Greenwich.

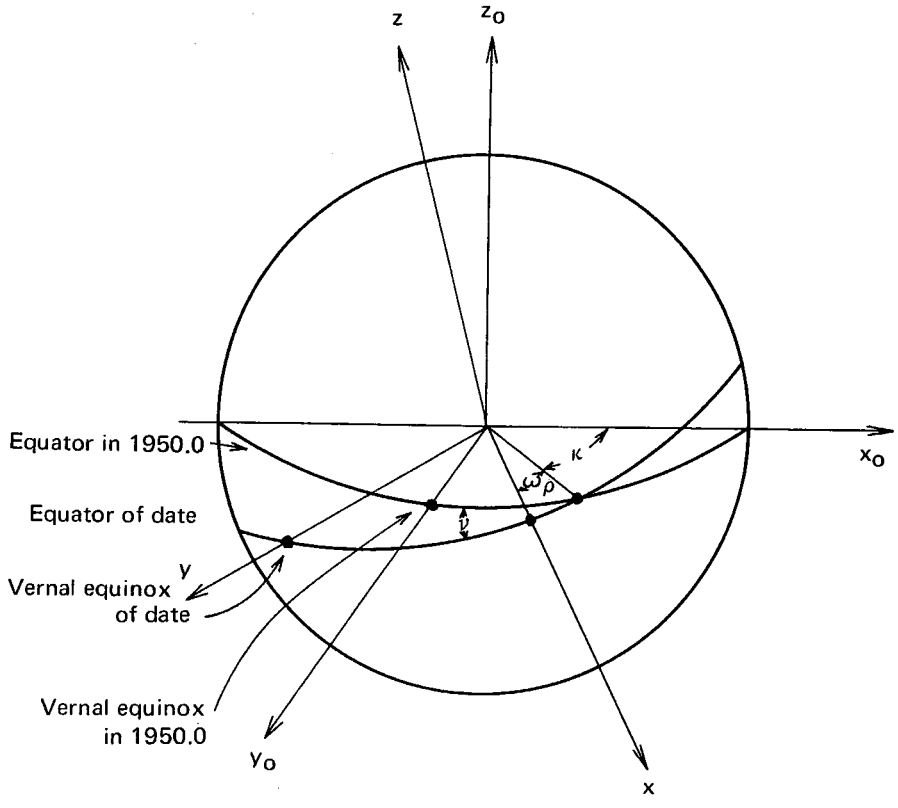

Fig. 1-8 Precession κ, ω_ρ, ν. The coordinates x, y, z, are referred to the equator of date and x_o, y_o, z_o are referred to the equator in 1950.0.

Celestial radio source positions are typically recorded in terms of right ascension and declination relative to the mean equator and equinox of 1950.0, so that these are transformed to the coordinates of date. If **P** and **N** represent the rotation matrices of precession and nutation respectively, then the desired apparent source position $\vec{S}$ is given by

$$\vec{S} = \mathbf{P} \cdot \mathbf{N} \cdot \vec{S}_{1950} \quad \cdots\cdots \quad (1.76)$$

where $\vec{S}_{1950}$ is the source position in 1950.0, mentioned above. The matrix **P** is give by

$$\mathbf{P} = \begin{pmatrix} \cos(\omega_p) & -\sin(\omega_p) & 0 \\ \sin(\omega_p) & \cos(\omega_p) & 0 \\ 0 & 0 & 1 \end{pmatrix} \cdot \begin{pmatrix} \cos(\nu) & 0 & -\sin(\nu) \\ 0 & 1 & 0 \\ \sin(\nu) & 0 & \cos(\nu) \end{pmatrix}$$

$$\cdot \begin{pmatrix} \cos(\kappa) & -\sin(\kappa) & 0 \\ \sin(\kappa) & \cos(\kappa) & 0 \\ 0 & 0 & 1 \end{pmatrix} \quad \cdots\cdots\cdots\cdots\cdots\cdots\cdots\cdots (1.77)$$

where κ, ω_p and ν are defined in Fig. 1-8. The matrix **N** is given by

$$\mathbf{N} = \begin{pmatrix} 1 & -\Delta\psi\cdot\cos(\epsilon_o) & -\Delta\psi\cdot\sin(\epsilon_o) \\ \Delta\psi\cdot\cos(\epsilon_o) & 1 & -\Delta\epsilon \\ \Delta\psi\cdot\sin(\epsilon_o) & \Delta\epsilon & 1 \end{pmatrix} \quad \cdots\cdots (1.78)$$

where $\Delta\psi$ is the nutation in longitude, $\Delta\epsilon$ is the nutation in obliquity and ϵ_o is the true obliquity of date of the ecliptic.

2. Accurate Real-time VLBI System

Fig. 2-1 shows the block diagram of the accurate real-time VLBI system. Although this system covers two frequency bands, one from 4030 to 4130 MHz and the other from 31600 to 32600 MHz, observations were carried out mainly at 4 GHz band because of the phase instability at 32 GHz band. For this reason, we mainly describe the system of 4 GHz band.

2.1 Antenna and receiver

All antennas used in our VLBI system have Az-El mount and the intersecting point of the Az and El axes, as shown in Fig. 2-2, does not move even if the direction of the antenna beam is changed. Therefore, it is convenient to define the intersecting point as the reference point of a baseline. Then, we describe the difference between the ideal reference point and the actual point. An antenna has its azimuth-axis tilt (x), elevation axis skew (ϵ) and collimation error (δ). They cause the errors in the reference point. These errors are given by

$$\begin{aligned} \Delta\ell_1 &\sim x\cdot\ell_1 \\ \Delta\ell_2 &\sim \epsilon\cdot\ell_2 \\ \Delta\ell_3 &\sim \delta\cdot D \end{aligned} \quad \cdots\cdots\cdots\cdots\cdots\cdots\cdots\cdots\cdots\cdots\cdots\cdots\cdots\cdots (2.1)$$

where $\Delta\ell_i$ is the position error due to each cause. Usually x, ϵ and δ are less than several thousandth degree, and ℓ_i and D is several tens m, so that these errors are far less than 3 cm which corresponds to the delay time measurement accuracy and have no influence on VLBI observations.

The choice of an antenna and an RF amplification system for VLBI depends on several factors including an antenna diameter, receiver noise, phase stability and bandwidth. The significance of these factors depends on the particular requirements of a given experiment, but the antenna diameter and receiver noise are commonly most important. Usually the minimum detectable flux density about 1 J_y (1 $J_y = 10^{-26}$W m^2 Hz^{-1}) is required for the applications to geodesy and astrometry. Fig. 2-3 shows the relation between the integration time and the antenna diameters, when $\sigma_\phi = 0.1$ radian, $S_o = 1$ J_y, $\eta_x = \eta_y = 0.6$, $B = 2\times 10^6$

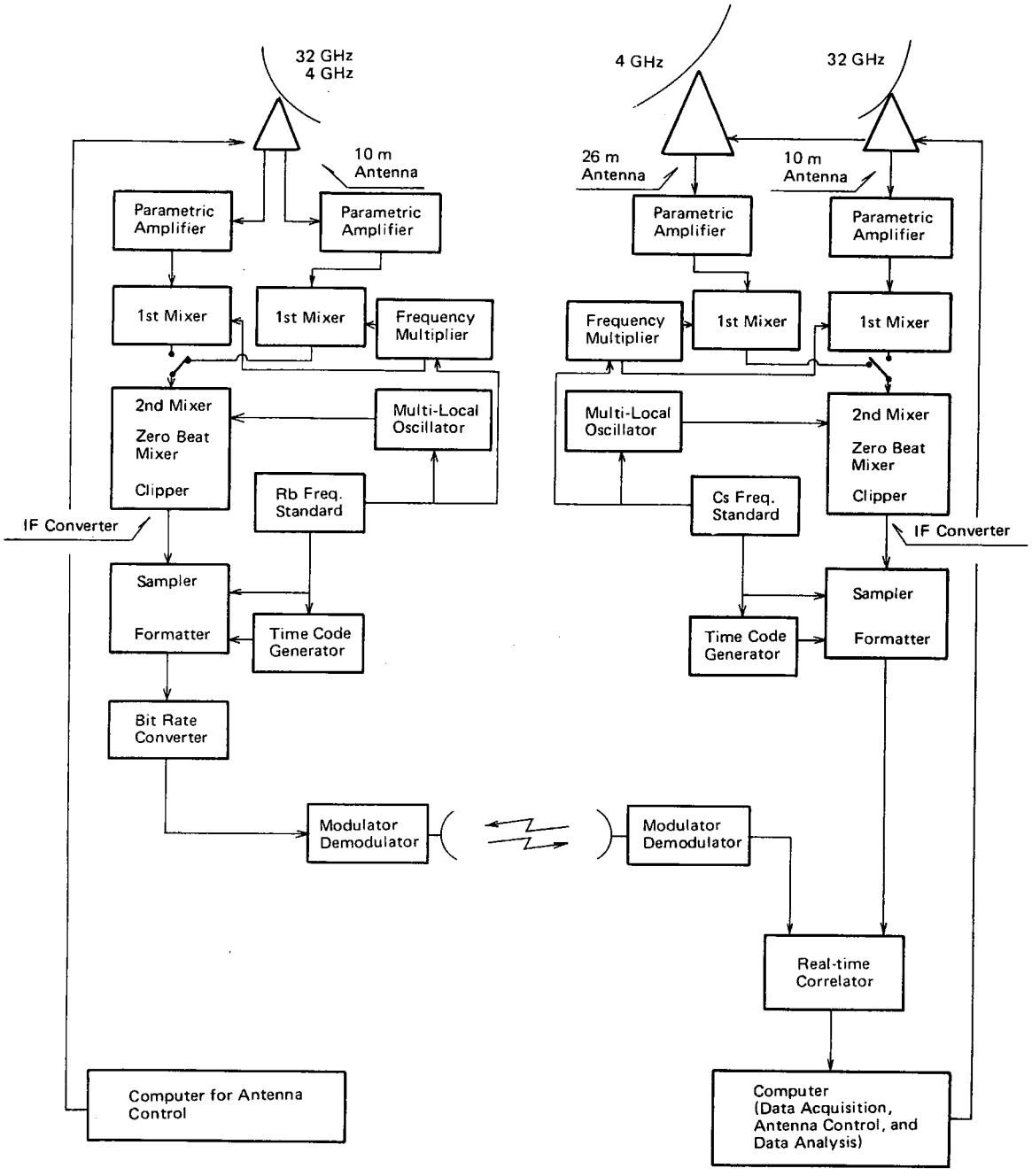

Fig. 2-1 Real time VLBI system

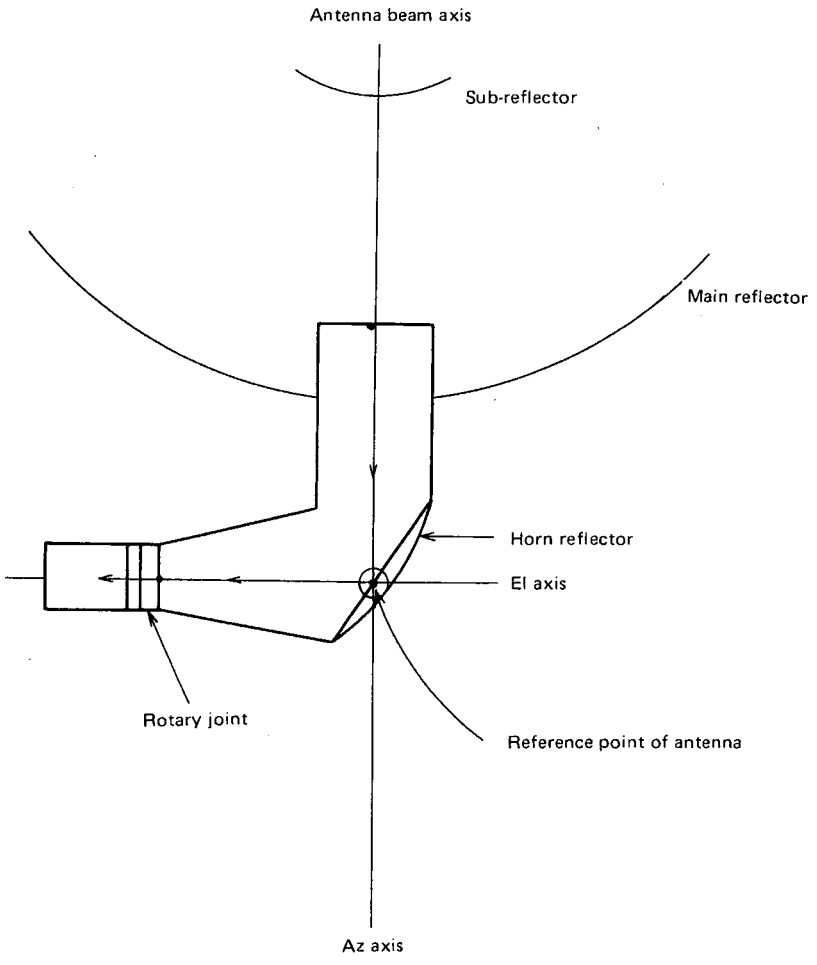

Fig. 2-2 26 meter antenna and reference point of the antenna

Hz, $D = D_X = D_Y$ and $T_S = T_{SX} = T_{SY}$ in Equation (1.66). As is evident from Equation (1.66), the integration time required obeys the 4th power law of the antenna diameter and the 2nd power law of the system noise temperature, so that the VLBI system needs a large antenna and a low noise amplifier. Our system employs a 26 m antenna for exclusive 4 GHz use at the main station and two 10 m antennas at both stations, and an uncooled parametric amplifier with a receiver noise temperature of about 45 K and a cooled parametric amplifier with a noise temperature of about 165 K are used at 4 GHz and 32 GHz respectively. Table 2-1 shows the performances of the antenna and receiver of our system.

The phase stability of the low noise amplifier is primarily important. Fig. 2-4 is an example of the frequency-phase (delay) characteristic. Usually a low noise amplifier has deviations of 0.1 ns or less over 100 MHz frequency band, but the deviations within one channel of a few MHz band are far smaller than 0.1 ns. However, fortunately these deviations can be calibrated and corrected by the phase difference between channels θ_k's in Equation (1.54). Therefore, only the time variations of θ_k between consecutive two phase differences directly influence the delay time measurement accuracy. Fig. 2-5 gives the phase

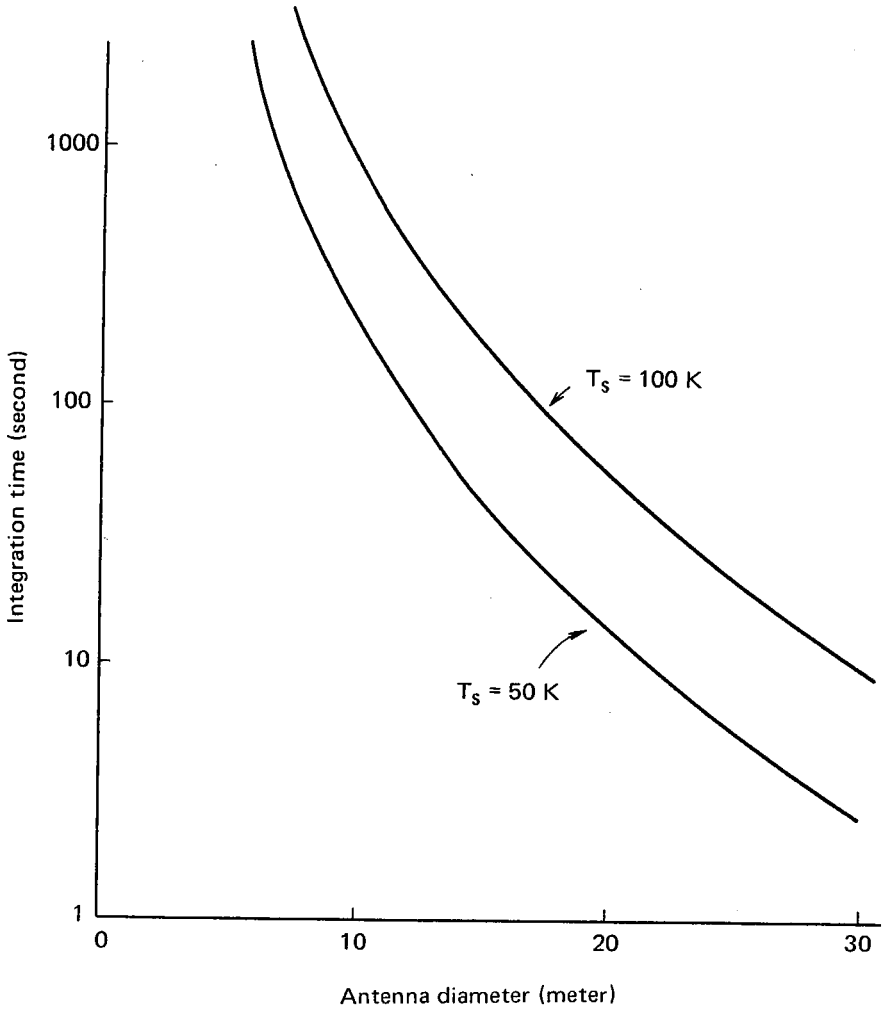

Fig. 2-3 Integration time required for phase detection.

Table 2-1 Performances of the antennas and receivers.

		Main-station	Sub-station
Antenna diameter	4 GHz	26 m	10 m
	32 GHz	10 m	(for both freq.)
Antenna noise temperature	4 GHz	22 K	51 K
	32 GHz	102 K	117 K
Receiver noise temperature	4 GHz	49 K	44 K
	32 GHz	130 K	130 K
Pre-amp. gain	4 GHz	62 dB	60 dB
	32 GHz	34 dB	34 dB
J_y/K	4 GHz	8.0	78.4

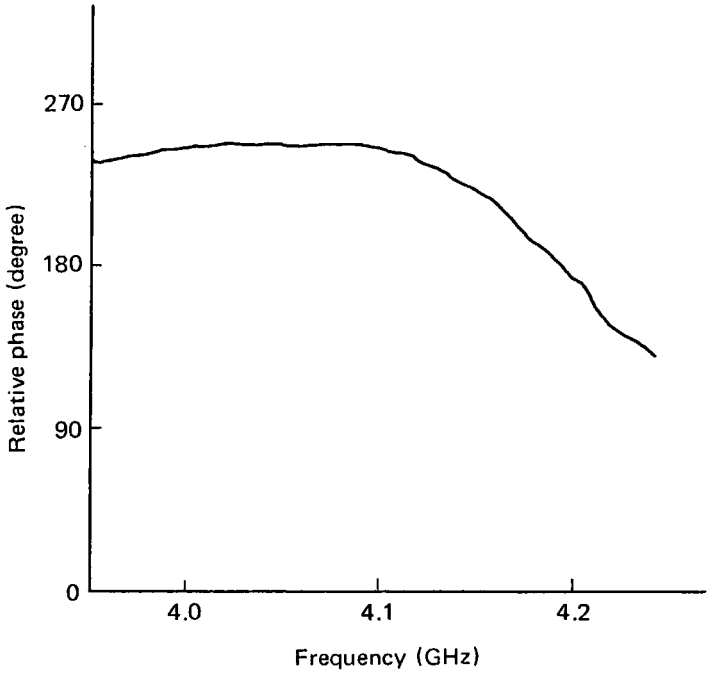

Fig. 2-4 Phase-frequency characteristic of the low noise amplifier. Relative phase of 360 deg. corresponds to 0.25 ns at 4 GHz.

stability of the uncooled parametric amplifier at 3950 MHz. The phase variation is within 1 deg. and this value causes merely 0.03 ns delay time error in the synthesis of 100 MHz bandwidth.

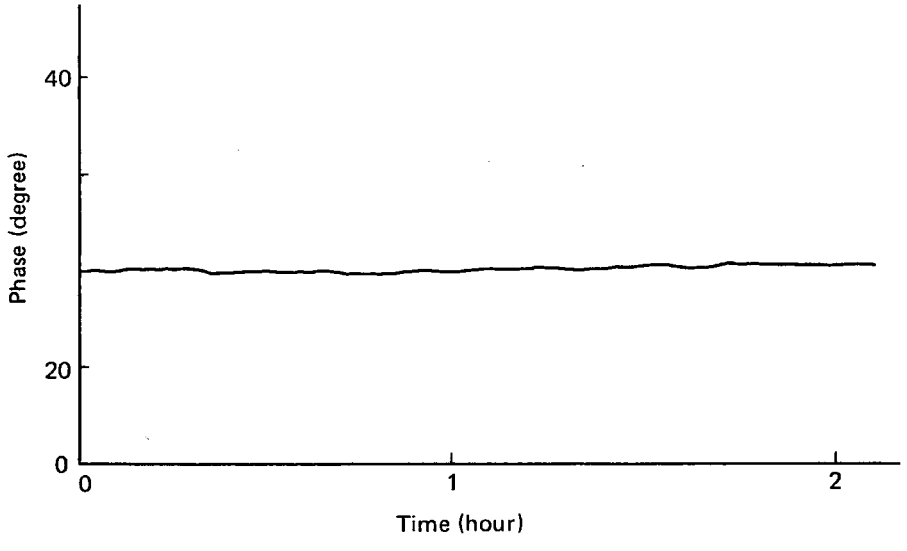

Fig. 2-5 Phase stability of the low noise amplifier at 3950 MHz.

2.2 Frequency converter and frequency standard

A frequency converter plays an important role in a VLBI system. This role is to frequency-convert RF signals received at the two independent stations to video ones so as to keep the coherence between the two signals. The short term phase noise due to the frequency converter causes a reduction of correlation amplitude or coherence, and the long term phase noise also causes the delay time error, the so-called time synchronization error. Therefore, the performance characteristics of the frequency converter, in large part, determine the success or failure of an experiment.

A frequency converter consists of mixers, a local oscillator system with a frequency standard etc. High frequency VLBI local oscillator generally has two types. The first type is the direct multiplication from a lower frequency reference, and the second is the so-called PLO (phase-locked oscillator). In both cases, the high stability of the reference is required in VLBI system, and usually atomic frequency standards such as Rb, Cs and H-maser are used as the reference sources. In our system, high performance Cs and Rb frequency standards are adopted for economical reason. While Fig. 2-6 shows the frequency stabilities of the two standards and Fig. 2-7 gives the phase noises derived from the frequency stabilities and the results obtained by receiving the geosynchronous satellite (CS) at rather high elevation angle. The results of receiving CS include not only the phase noise due to the frequency converter but the tropospheric phase scintillations, so that the phase noise may be less than these values. The phase noise in Fig. 2-7 increases with the mean time (integration time). Considering that the phase noises at the two stations are mutually independent, the coherence may

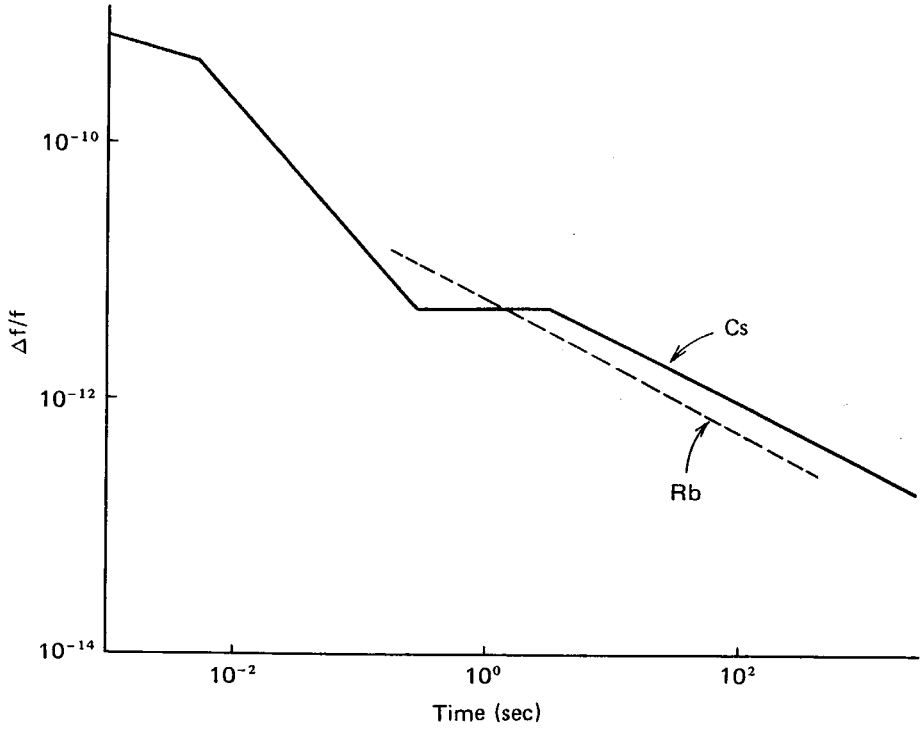

Fig. 2-6 Frequency stabilities, Δf/f, of the atomic frequency standards.

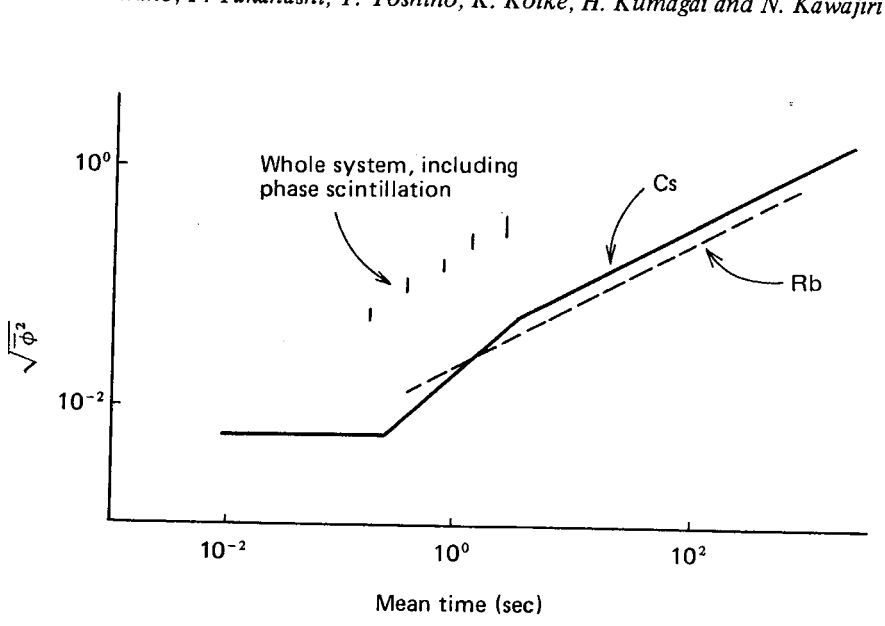

Fig. 2-7 Phase noise due to the atomic frequency standard and phase variation due to the whole system, including phase scintillations.

decrease with the long integration time. Practically, the integration time is limited to about 20 sec. in our system.

Fig. 2-8 shows the block diagram of the local chain of our system. In the multi-down converter, the receiving channel separated by 0, 10, 30, 60, 100 MHz can be switched sequentially every 10 ms by changing the local frequency in order to perform the band-width synthesis. The multi-down converter has two features which are demanded for its use as a switched-frequency local oscillator. The first is that the output frequency can be electrically selected, allowing it to be controlled by an external digital controller. And secondally, the internal electronics of the local oscillator are such that, upon switching from one frequency to another and then back again, the phase returns to the same value which it would have had as if the frequency had been never changed. It is possible to extrapolate

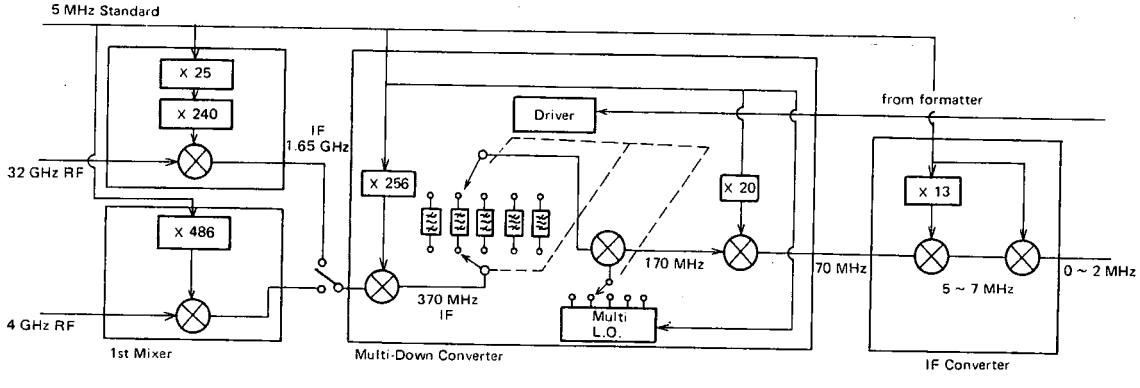

Fig. 2-8 Local chain of the real-time VLBI system.

the fringe phase from one channel to the next and hence synthesize an apparent bandwidth equal to the largest separation of the receiving frequency.

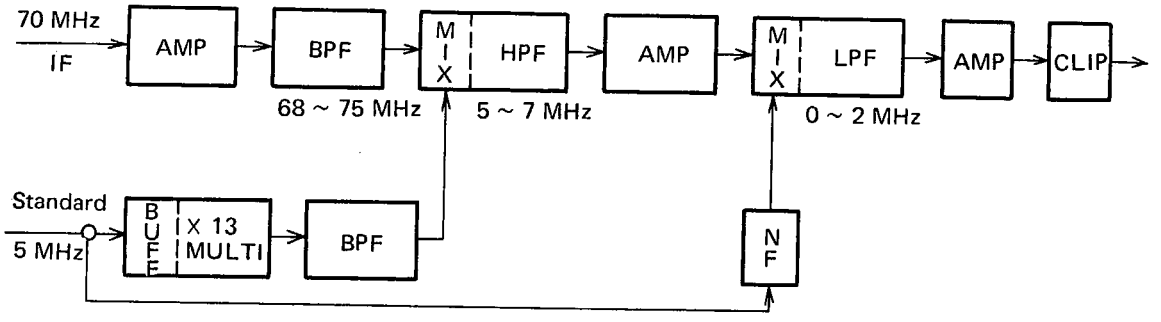

Fig. 2-9 Block diagram of IF converter.

The IF converter block diagram is shown in Fig. 2-9. The main function of this unit is to shift a band of data centered at an IF frequency down to the video range. The important parts of the IF converter are a high-pass filter (HPF) and a low-pass filter (LPF). The HPF and LPF give the frequency-amplitude and frequency-phase (delay) characteristics in the lower frequency range and upper range respectively. Fig. 2-10 shows an example of the two characteristics through the multi-down converter and the IF converter. The deviations of the two characteristics on both sides of the 2 MHz video band are caused by the HPF and LPF respectively. These deviation may cause an error in the delay time estimation, and hence the data for 150 kHz band at both sides in the video range are removed. We also consider these effects of HPF and LPF during data processing.

The last stage of the IF converter is a clipper which takes the video signal and clips it into a square wave signal. The signal clipped here are one-bit-sampled in the formatter. In one-bit-sampling, when the signal level stays above the positive threshold, the sampler determines the signal to be one. On the other hand it determines that to be zero or minus one when the signal stays below the negative threshold. However, when the signal level stays between positive and negative thresholds, the sampler does not always sample the signal correctly. The sampling in such case is called "mis-sampling". One may use a amplifier with high gain before the sampler in order to avoid the mis-sampling.

Supposing that the signal is a Gaussian random noise, the probability of the signal to stay between V and V + dV in voltage is given by[21]

$$p(V)\,dV = (1/-2\pi V^2_{eff}) \cdot \exp(-V^2/2V^2_{eff}) \cdot dV \quad \cdots\cdots\cdots\cdots\cdots\cdots \quad (2.2)$$

where V_{eff} is the effective voltage of the signal. This signal being amplified by voltage gain G, the probability to stay between $-V_O$ and $+V_O$ in voltage is given by

$$P(V_O) = \int_{-V_O}^{V_O} \exp(-V^2/2G^2 \cdot V^2_{eff}) / (G \cdot \sqrt{2\pi V^2_{eff}}) \cdot dV \quad \cdots\cdots\cdots \quad (2.3)$$

$$\sim 2V_O/G \cdot \sqrt{2\pi V^2}_{eff} \quad \cdots\cdots\cdots\cdots\cdots\cdots\cdots\cdots\cdots\cdots \quad (2.4)$$

where we suppose that G is large enough. When V_O is equal to V_{eff}, we rewrite Equation (2.4) as

$$P(V_{eff}) \sim \sqrt{2}/(\sqrt{\pi}G) \quad \cdots\cdots\cdots\cdots\cdots\cdots\cdots\cdots\cdots\cdots \quad (2.5)$$

From Equation (2.5), we can obtain the following results. The voltage gain G must be more than 20 dB in order to reduce the probability of mis-sampling to less than 1%.

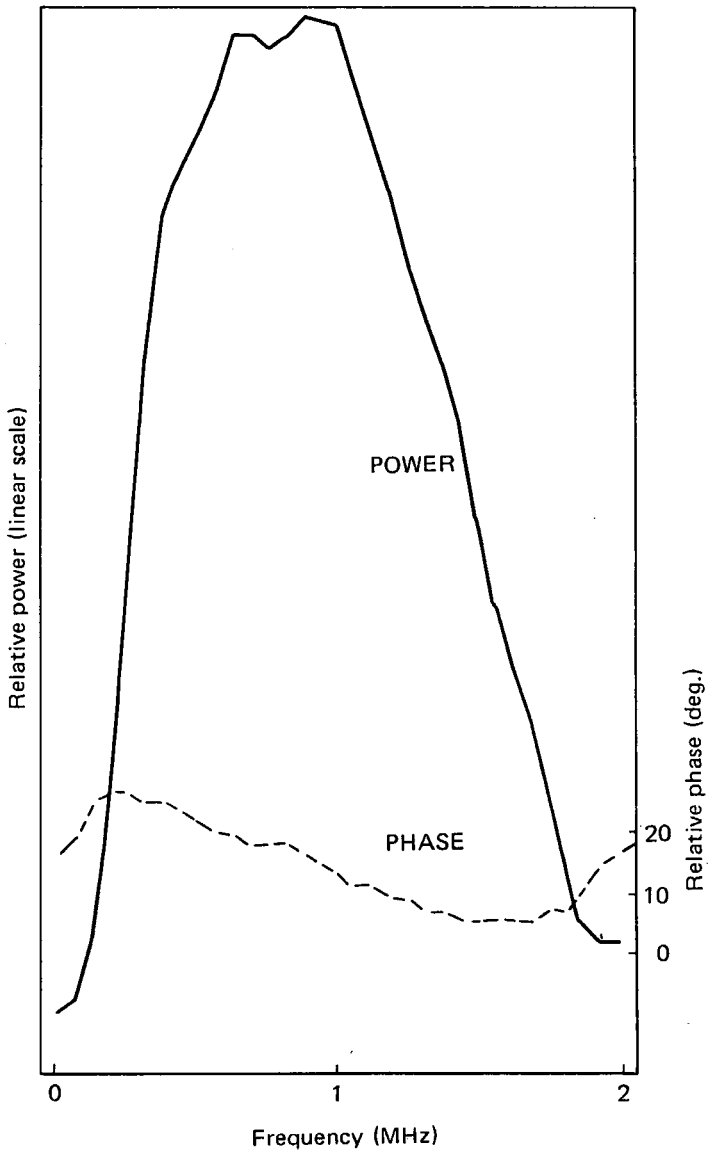

Fig. 2-10 Frequency-power and frequency-phase characteristics through the multi-down converter and the IF converter.

2.3 Formatter

The formatter samples the clipped video signal and arranges the data into 100 blocks of a second called frames. The arrangement of data is shown in Fig. 2-11. The frame starts out with a sync word which consists of six 0111 patterns, and then there are four 01 patterns to mark the beginning of a frame. The sync word is needed to allow the decoder in the correlator to locate the frame boundaries and hence to decode the data. The start time of the sync word is just coincident with every 10 ms synchronized with the standard time which is generated by the atomic frequency standard at each station. Therefore, the timing of whole data can be referred to the data number which is counted from the sync word.

Fig. 2-12 shows the block diagram of the formatter. There are several frequencies used in the formatter. The phase-lock control unit generates 4 MHz and 4.096 MHz synchronized with 1 MHz from the frequency standard and all the frequencies are generated from this

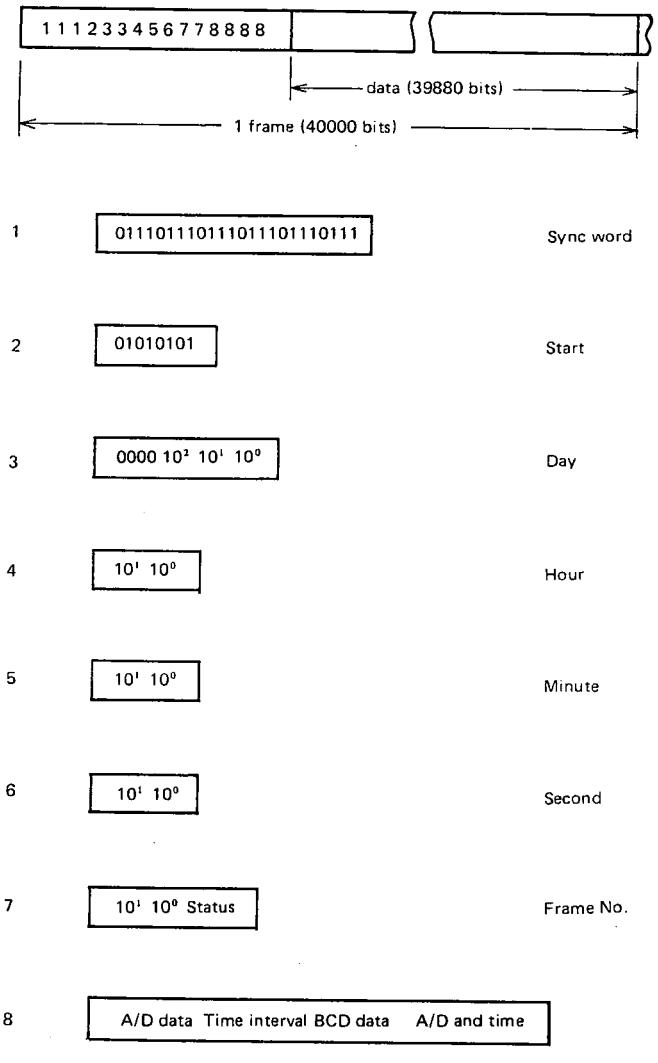

Fig. 2-11 Arrangement of data

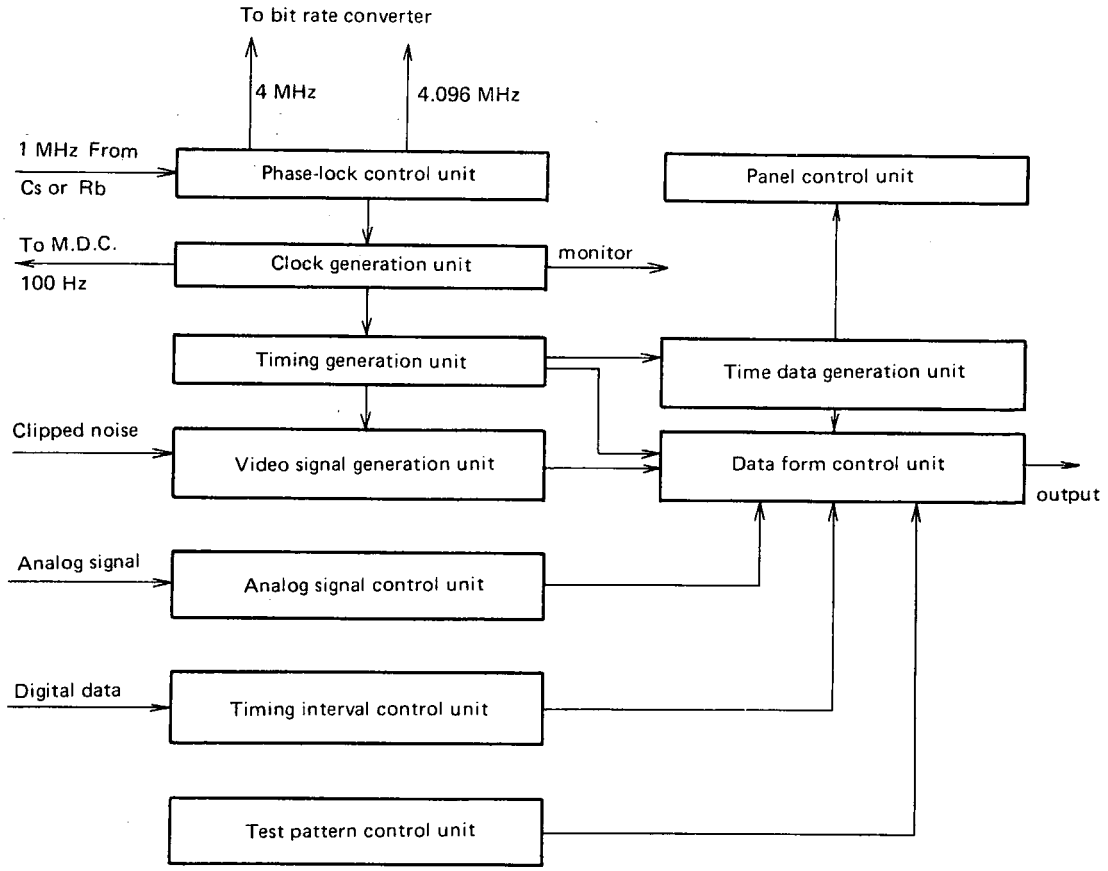

Fig. 2-12 Block diagram of the formatter.

4 MHz. The 4.096 MHz signal, on the other hand, is used for transmission by a microwave link. The clock generation unit and timing generation unit generate all the clocks and timing signals which are needed to control the data, and synchronize with the 4 MHz and hence with the atomic frequency standard. One of the most important clocks is a sampling clock. Incomplete synchronization in the sample timing at each station causes the phase change proportional to the video frequency of $0 \sim 2$ MHz and hence causes the change of the delay time. For example, when the delay of sample timing is 10 ns, the phase of 2 MHz is delayed by about 7 degrees. This phase delay causes the error of about 0.1 ns in the delay time estimation by the method of the bandwidth synthesis. For this reason, the variations of sample timing are limited to less than several ns in our system.

The video signal generation unit samples the clipped video signal and outputs the digital data to the data form control unit. The analog signal control unit and timing interval control unit replace analog data and digital data with a part of the sampled data stream respectively, and the test pattern control unit is also used to exchange the sampled data for test data. The panel control unit controls the display on the front panel, and the time data generation unit produces time codes which are also displayed on the front panel and are inserted into the data stream.

2.4 Microwave link

In the real-time VLBI system, the terrestrial microwave link plays an important role. The link transmits the data formatted at the sub-station in real time, and hence it allows the real-time correlator to perform data processing immediately. However, while the bit rate of the formatted data stream mentioned above is 4.0 mega bits/sec. (bps), the transmission rate is 4.096 Mbps, which is the inherent bit rate in the microwave link. The bit-rate converter at the sub-station, therefore, converts the bit rate to 4.096 Mbps. The bit rate converter has two random access memories (RAM), as shown in Fig. 2-13. Each RAM consists of 64 kbit memories. No. 1 RAM stores the first frame which consists of 4×10^4 bits, and then outputs these 4×10^4 bits and 960 dummy bits from No. 1 RAM to the microwave link at the rate of 4.096 Mbps while the next frame enters No. 2 RAM. Next, we output 4.096×10^4 bits from

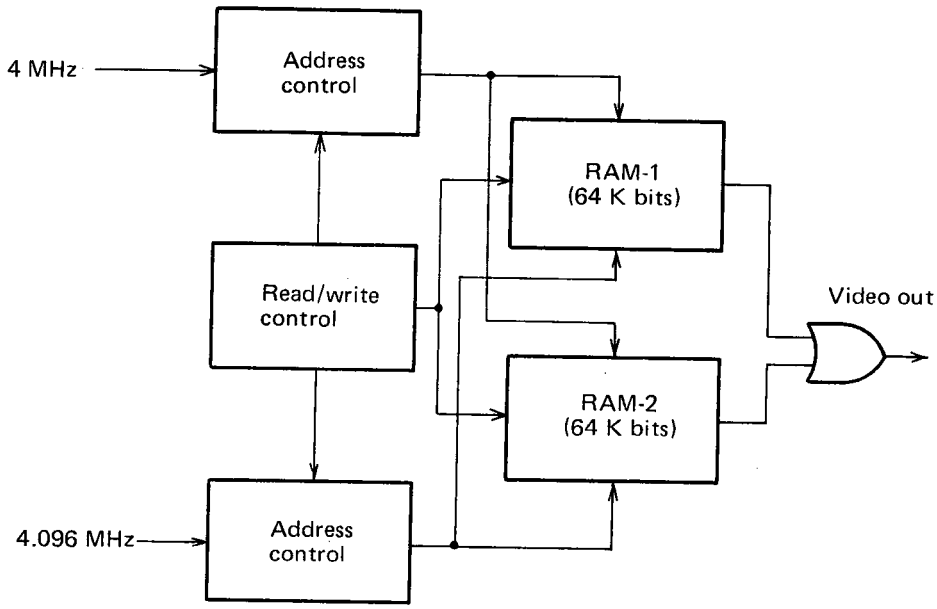

Fig. 2-13 Block diagram of the bit rate converter.

No. 2 RAM, while the following frame enters No. 1 RAM. Such process is performed in a cyclic fashion. The extra 960 bits for a frame are called the dummy bits and may be removed in the real-time correlator.

Let us consider on the increase of bit error rate (BER) due to rain or other precipitation. The intense fading at 7 GHz band which is used in our microwave link often occurs due to precipitation. Fig. 2-14 shows the percentage of time abscissa is exceeded. Our microwave link has the margin 25dB for BER = 10^{-6}. From Fig. 2-14 the probability of attenuation to exceed 25 dB is less than 0.1%, so that the probability of BER more than 10^{-6} is less than 0.1%. Thus, rain or other precipitation have no severe influence on the increase of BER in our microwave link.

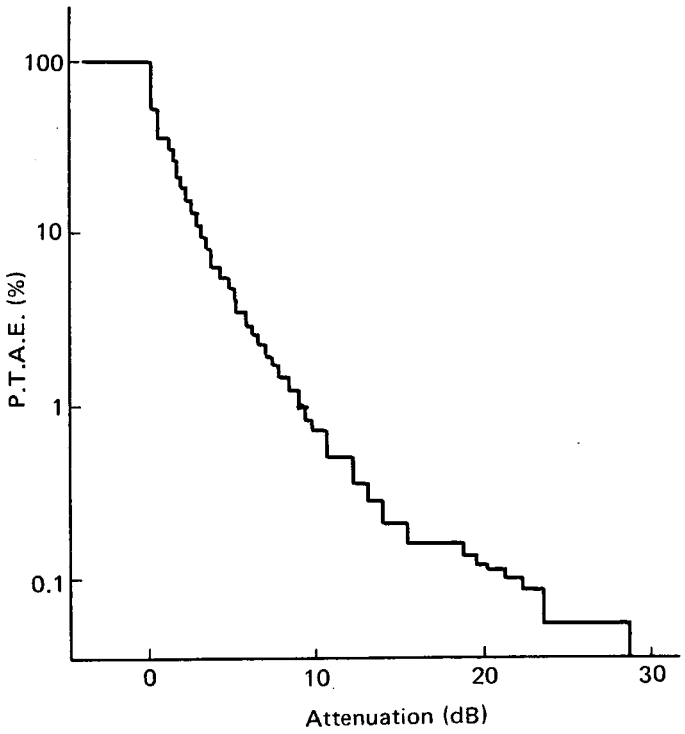

Fig. 2-14 Percentage of time abscissa is exceeded, (P.T.A.E.).

2.5 Real-time correlator

The real-time correlator cross-correlates the data streams, rotates the fringes, displays the cross-correlation functions and outputs these functions into the mini-computer via direct memory access. The correlation, along with the fringe rotation or stopping, is performed on a frame basis, and the cross-correlation functions integrated for 10 ms (one frame) are collected into the mini-computer every 10 ms.

Fig. 2-15 shows the block diagram of the real-time correlator and the mini-computer, and Fig. 2-16 shows the flow of data reduction.

The real-time correlator has a particular function to process the data streams in real time. There must be corrected the transmission delay due to the microwave link, time synchronization error, etc. The delay correction is achieved by four buffer memories. The whole data of the first frame from the main station are stored in RAM 1 and the data from the sub-station in RAM 3. Next, the data from the two stations are also stored separately in RAM 2 and RAM 4, while the data in RAM 1 are sequentially output from the first address and the data in RAM 3 from the address shifted by the bits which corresponds to the total delay time. Such process is performed in a cyclic fashion. The number to be shifted is calculated before this processing.

The data streams and the clocks from the two stations go into the correlator, and then the sync words are detected. After the sync word detection, the whole data following the sync word are stored into a RAM. The data stream shifted by m bits mentioned above goes

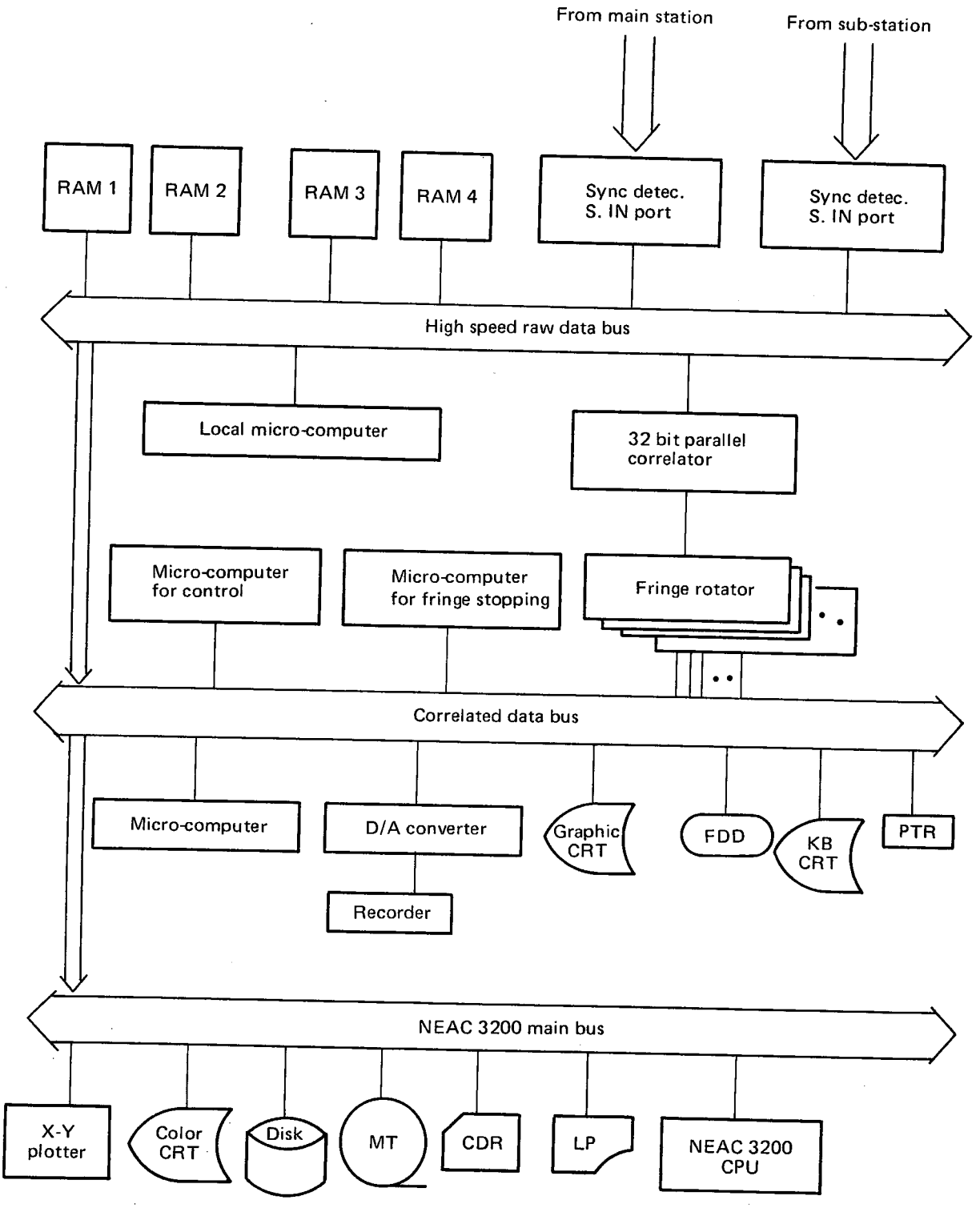

Fig. 2-15 Block diagram of the real-time correlator and the mini-computer NEAC 3200.

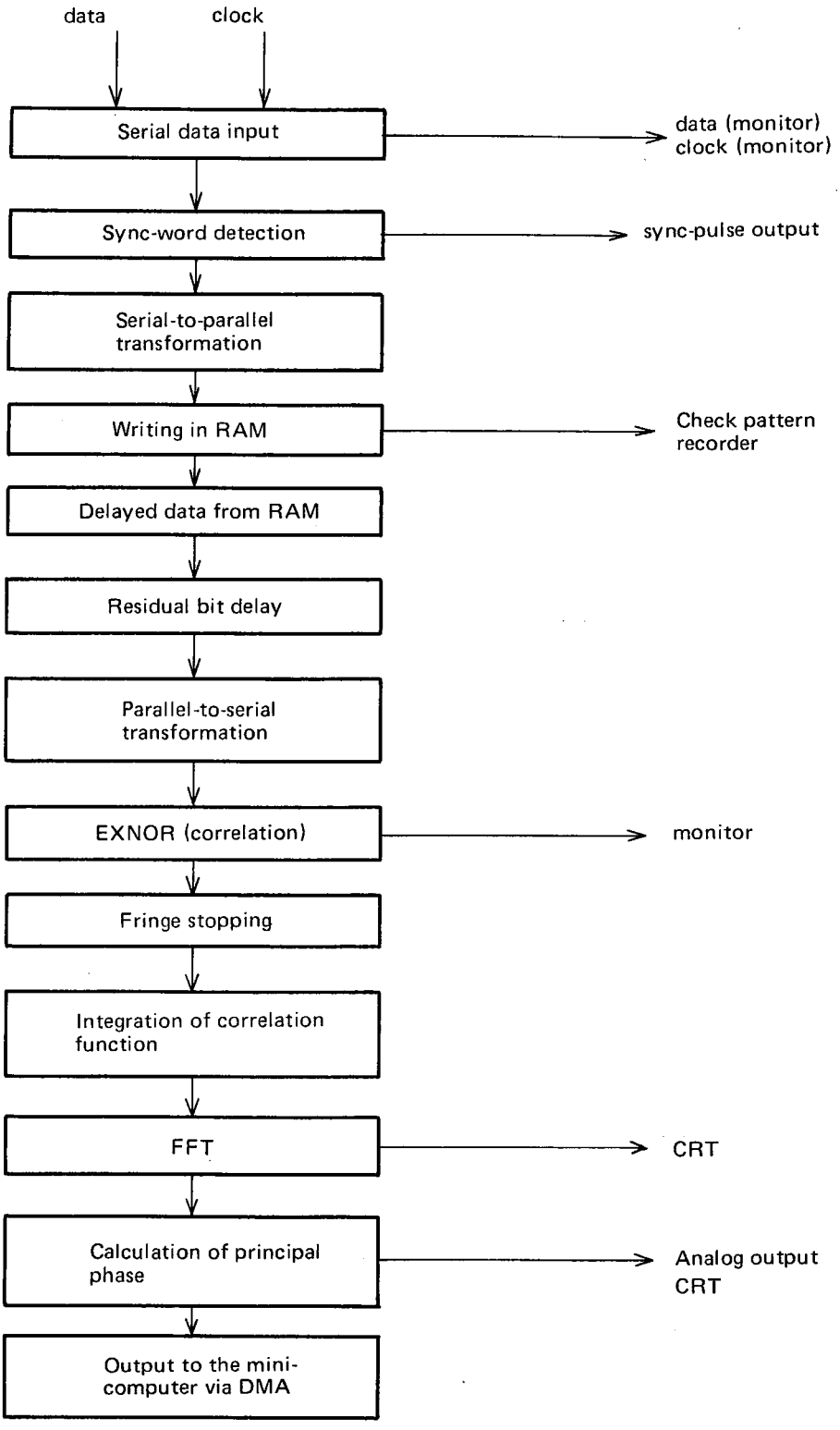

Fig. 2-16 Flow of data reduction in the real-time correlator.

into 32 bit parallel correlator for the sub-station. On the other hand, the data stream from RAM for the main station directly enter the 32 bit correlator. The output from the ℓth shift-register in the correlator for the sub-station is $y(n+m+\ell)$, while the data stream for the main station is $x(n)$. The two data stream are correlated by EX-NOR devices in the correlator. The cross-correlation function is given by

$$R_{xy}(\ell)_i = \sum_{n_i+1}^{n_{i+1}} x(n) \cdot y(n+m+\ell) \quad \cdots\cdots\cdots\cdots\cdots\cdots\cdots\cdots \quad (2.6)$$

where

$$\ell = -16, -15, \ldots\ldots, 0, \ldots\ldots, 14, 15$$

and m is the priori value assumed for the total delay time including the transmission delay in the microwave link, quantized in unit of the sample interval 250 ns. The complex correlation function obtained through the fringe stopping, $r''_c(\ell)_i$ and $r''_s(\ell)_i$ are approximated by

$$\begin{aligned} r''_c(\ell)_i &= R_{xy}(\ell)_i \cdot \{I\} \\ r''_s(\ell)_i &= R_{xy}(\ell)_i \cdot \{J\} \end{aligned} \quad \cdots\cdots\cdots\cdots\cdots\cdots\cdots\cdots \quad (2.7)$$

From Equations (1.43), (1.44) and (1.45), the complex correlation function integrated for one frame (10 ms) is given by

$$\begin{aligned} r'_c(\ell) &= \sum_{n_i} r''_c(\ell)_i \\ r'_s(\ell) &= \sum_{n_i} r''_s(\ell)_i \end{aligned} \quad \cdots\cdots\cdots\cdots\cdots\cdots\cdots\cdots \quad (2.8)$$

where N is the number of data in one frame, namely about 4×10^4.

The familiar Van Vleck clipping correction[18] is applied to the corresponding parts of the correlation functions of a clipped signal, $r'_c(\ell)$ and $r'_s(\ell)$

$$\begin{aligned} r_c(\ell) &= \left(\frac{\beta}{MN}\right) \sin\left[\frac{\pi}{2} r'_c(\ell)\right] \\ r_s(\ell) &= \left(\frac{\beta}{MN}\right) \sin\left[\frac{\pi}{2} r'_s(\ell)\right] \end{aligned} \quad \cdots\cdots\cdots\cdots\cdots\cdots\cdots\cdots \quad (2.9)$$

where β and M are the same quantities as mentioned in Chapter 1. The complex correlation functions are displayed on a CRT and also transmitted to the host computer (NEAC 3200) with the aid of a micro-computer via direct memory access. The complex correlation function is transformed to the frequency domain in real time, and we can obtain the cross-spectral function as

$$S_{xy}(k) = \sum_{\ell=-32}^{31} R_{xy}(\ell) \cdot \exp[-i\pi\ell k/32] \quad \cdots\cdots\cdots\cdots\cdots\cdots \quad (2.10)$$

The phase at the 16th frequency is given by

$$\varphi(16) = \tan^{-1} [\mathrm{Im} \{ S_{xy}(16) \} / \mathrm{Re} \{ S_{xy}(16) \}] \quad \ldots\ldots\ldots\ldots \quad (2.11)$$

The 16th phase, $\varphi(16)$ is the frequency component at the center in the channel and is called a principal phase. The principal phases are continuously displayed on the CRT for 60 sec. Thus, we can monitor the status of the system such as the phase stability or phase scintillation through the display of principal phases during an observation.

2.6 Time Synchronization

Because the correlation is performed over 16 lags (±2 ms), we should know an initial value of the total delay time in unit of the sample interval, 250 ns, in order to begin data processing with the real-time correlator. However, while the instrumental and geometrical delay times can be predicted with a required accuracy of ±250 ns (one bit) and the propagation time is far less than 250 ns, we cannot know a time synchrnozation error because of its variation unless we measure it before a series of observations.

It is rather easy to measure the time synchronization error with a microwave link. The first bit of sync word is coincident with every 10 ms and synchronized with a standard time at each station. If the formatted data are exchanged via microwave link, we can measure the delay time between the two first bits of one station and the other. Assuming that ΔT_x and ΔT_y are the delays measured at the respective stations, the time synchronization error ΔT is given by

$$\Delta T = (\Delta T_x - \Delta T_y)/2 \quad \ldots\ldots\ldots\ldots\ldots\ldots\ldots\ldots\ldots\ldots \quad (2.12)$$

because

$$\Delta T_x = T_y + T_\mu - T_x$$
$$\Delta T_y = T_x + T_\mu - T_y$$

where T_x and T_y are the times at the stations x and y respectively. The transmission time in the microwave link T_μ is also obtained as

$$T_\mu = (\Delta T_x + \Delta T_y)/2. \quad \ldots\ldots\ldots\ldots\ldots\ldots\ldots\ldots\ldots\ldots \quad (2.13)$$

Usually this measurement accuracy is about 10 ns so that it is sufficient for data processing.

2.7 Mini-computer and data acquisition software

The mini-computer (NEAC-3200) plays the role as a host computer. It records the complex cross-correlation functions, observation time, etc. on a digital magnetic tape and also performs the accurate program tracking for an antenna. The data acquisition software is applied to transfer the data from the real-time correlator into the mini-computer. The data acquisition software has three modes to obtain the data for the particular requirements of a given experiment. These are 1) correlation mode, 2) ordinary mode and 3) raw data mode. In the first mode, the complex correlation functions, observation time, etc. are recorded on a digital magnetic tape of the mini-computer at the rate of 7120 words/sec. In the second mode, only the principal phases, etc. are recorded at the rate of 72 words/sec. When we try

to analyze all the formatted data of two consecutive frames from each station, these data can be recorded on the digital magnetic tape in the raw data mode.

3. Measurements of Delay Time and Phase Scintillation

3.1 Measurements of delay time

After the fine fringe stopping, the phase Φ_o^k of the kth channel at $\omega = 0$ in Equation (1.50) becomes the following expression

$$\Phi_o^k = \omega_o^k \cdot \Delta\tau + \theta_k \quad \cdots\cdots\cdots\cdots\cdots\cdots\cdots\cdots\cdots\cdots \quad (3.1)$$

$$k = 1, 2, 3, 4, 5$$

If we observe a number of delay times, the phase difference between the jth and the 1st phases is given by

$$\Delta\Phi_{o,j}^k = \omega_o^k \, (\Delta\tau_j - \Delta\tau_1) \quad \cdots\cdots\cdots\cdots\cdots\cdots\cdots\cdots\cdots\cdots \quad (3.2)$$

$$j = 1, 2, \ldots\ldots\ldots$$

or we can rewrite Equation (3.2) as

$$\Delta\Phi_{o,j}^k = \omega_o^k \cdot \Delta^2\tau_j \quad \cdots\cdots\cdots\cdots\cdots\cdots\cdots\cdots\cdots\cdots \quad (3.3)$$

where

$$\omega_o^1 = 0 \quad (\times 2\pi\text{MHz})$$

$$\omega_o^2 = 10 \quad (\times 2\pi\text{MHz})$$

$$\omega_o^3 = 30 \quad (\times 2\pi\text{MHz})$$

$$\omega_o^4 = 60 \quad (\times 2\pi\text{MHz})$$

$$\omega_o^5 = 100 \quad (\times 2\pi\text{MHz})$$

and $\Delta^2 \tau_j$ denotes $\Delta\tau_j - \Delta\tau_1$, namely, the change of delay time for the period between the jth and the first observations. We note that the phase difference between channels, θ_k, is not included in Equation (3.3). But, of course, we can derive physical parameters in Equation (1.69) from the temporal change of $\Delta^2 \tau_j$ except the initial value of ($\tau_g + \tau_p + \tau_e + \tau_i$).

Fig. 3-1 shows $\Phi_{o,j}^k$ obtained by receiving QSO 3C273 for 20 sec., and hence a set of observations for five channels takes 10 sec. We can determine the delay time from the slope of the linear function, shown as a dotted line in Fig. 3-1, fitting the five phase differences by the method of least squares. Matsumoto[22] showed that the result by the method of least squares is equal to one by the most-likelihood estimate when a signal-to-noise ratio is large enough. We actually determined the differences by both methods, but we could not find the difference between two methods.

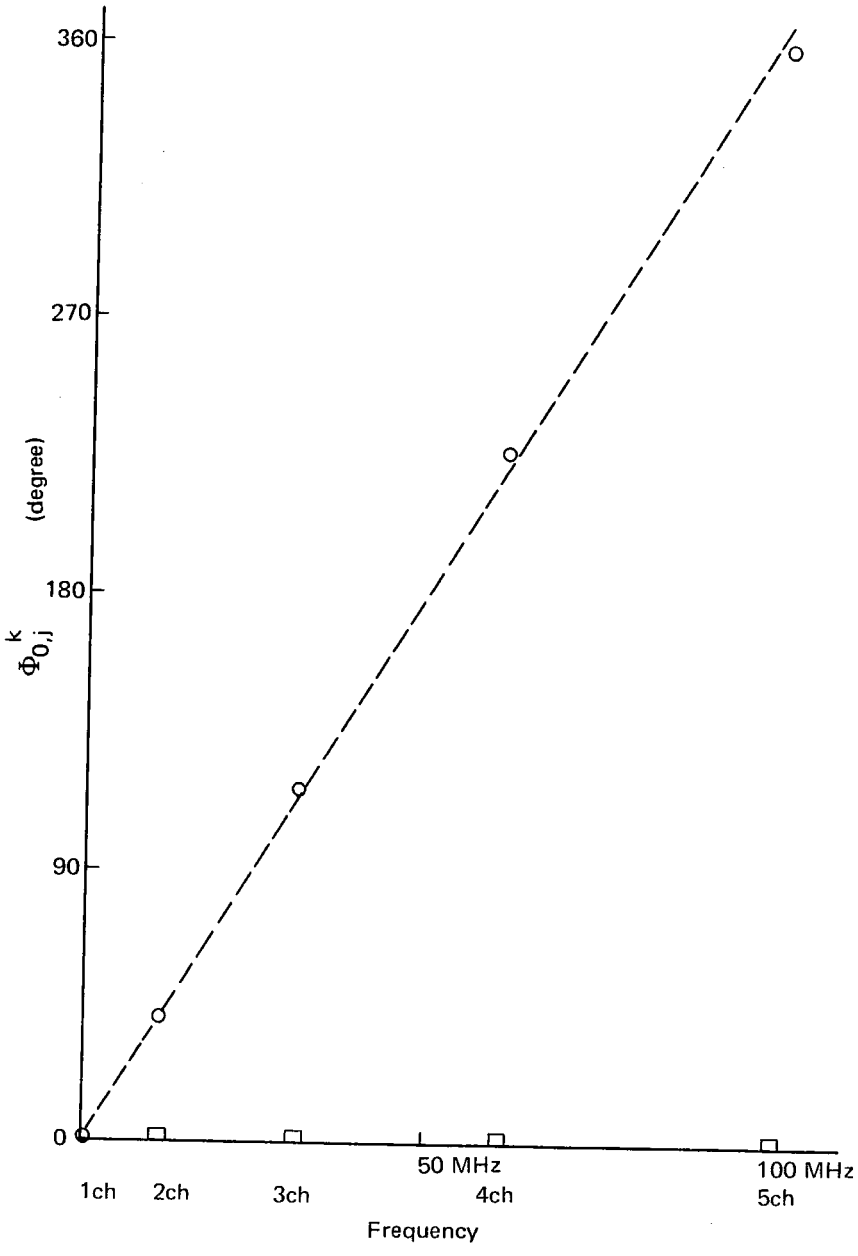

Fig. 3-1 Phase difference $\Phi_{0,j}^{k}$ obtained from 3C273.

There is an intense radio source available for the measurement of delay time with VLBI system, namely, communication satellite CS emitting radio waves at 4 GHZ over the wide bandwidth. We received this satellite and measured the change of delay time $\triangle^2 \tau_j$ every 100 ms (the integration time in each channel is equal to 20 ms) by the method of the minimum redundant bandwidth synthesis. Fig. 3-2 shows the change of delay time which is subtracted by the predicted values. The estimation error of the delay time was about 0.1 ns. For the 20 consecutive delay times, the peak-to-peak error and r.m.s. error were 0.27 ns and 0.08 ns

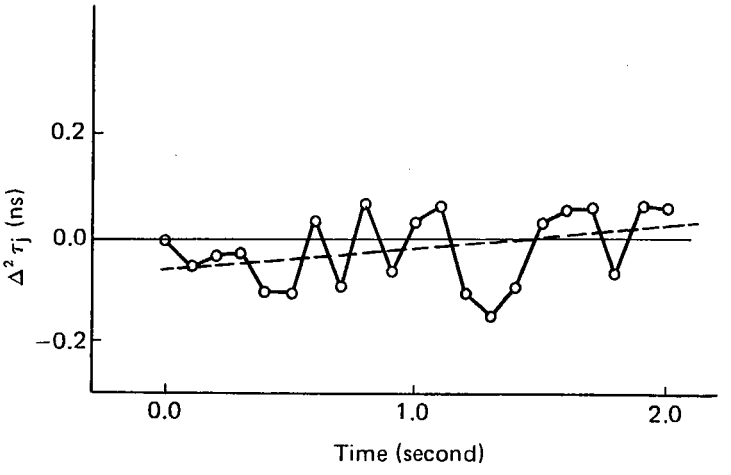

Fig. 3-2 Difference of delay times, $\Delta^2\tau_j$, obtained from CS.

respectively. However, the slow variation of about 0.02 ns/sec., shown as the dotted line in Fig. 3-2, superimposed on these data. These results indicate that the delay time measurement accuracy in our system is about 0.1 ns. The slow variation may be caused by the frequency standards and the rate of the slow variation is called differential "clock rate".

We also observed QSO 3C273 and measured the change of delay time $\Delta^2\tau_j$ every 10 sec. The integration time in each channel was 2 sec. The estimation error of delay time was about 0.17 ns by reason of insufficient integration time. Fig. 3-3 shows the results for 3C273 corresponding to Fig. 3-2. The difference between the observed and predicted values (O-C)

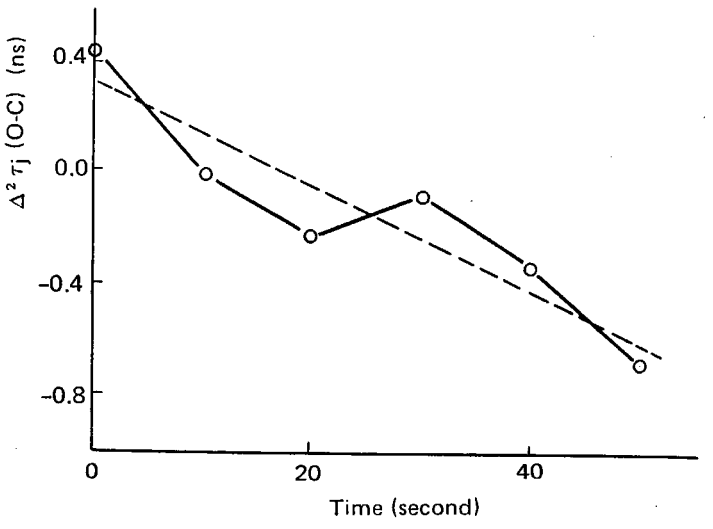

Fig. 3-3 Difference of delay times, $\Delta^2\tau_j$, (O-C) obtained from QSO 3C273.

indicates approximately linear change. This change is also caused by the clock synchronization error due to the frequency standards mentioned above. We can estimated differential clock rate to be about 0.025 ns/sec, as shown in Fig. 3-3. Fig. 3-4 shows a long term variation of the O-C. One can find the slow change of the slope, namely the change of the differential clock rate. Thus, it is clear that an H-maser frequency standards with frequency stability higher than 10^{-14} is required to observe a weak radio source by VLBI system.

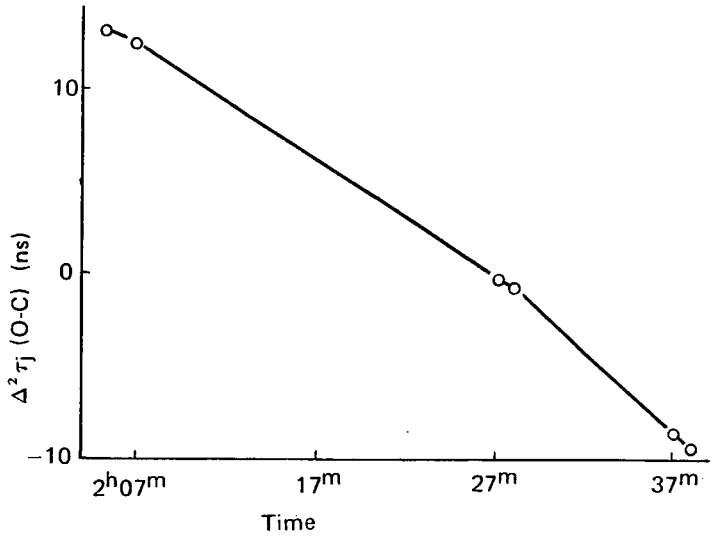

Fig. 3-4 Difference of delay times $\Delta^2\tau_j$ (O-C) obtained from QSO 3C273.

3.2 Measurements of phase variation

Phase variations observed by VLBI system include ones caused by the equipments, phase jitters of the frequency standards, data processing and phase scintillations due to the atmosphere. However, it can be assumed, for the results of our phase scintillation measurements and phase noises of Cs and Rb frequency standards given in Fig. 2-7, that the phase variations due to the phase noise and the phase scintillations are less than one deg. within the period of 0.5 sec. Therefore, observed phase variations within that period can be regarded as the phase variations due to equipments and data processing.

Fig. 3-5 shows a sample of the phase variation obtained by receiving CS, which are subtracted by the predicted values calculated from the orbit. The peak-to-peak error and r.m.s. error for 0.5 sec. are 8 and 3 degrees respectively. These are the phase variations due to the equipments and data processing. From these results, the phase measurement accuracy for a short term is about 3 deg., and this value is approximately coincident with the phase error which gives the delay time error of 0.1 ns by our method of the bandwidth synthesis with 100 MHz span.

3.3 Measurements of phase scintillation

The phase scintillations, which corresponds to the variation of $(\omega + \omega_0) \cdot \tau_p$ in Equa-

tion (1.21), along the path through the atmosphere were observed for the first time using the real-time VLBI system. We alternately received radio waves from synchronous satellites CS at El = 47.8 deg. and INTELSAT at El = 1.7 deg. to obtain the atmospheric phase scintillations. The effects of secondary waves, which reflect on the ground, can be assumed to be far less than ones of phase scintillations at both elevation angles[23].

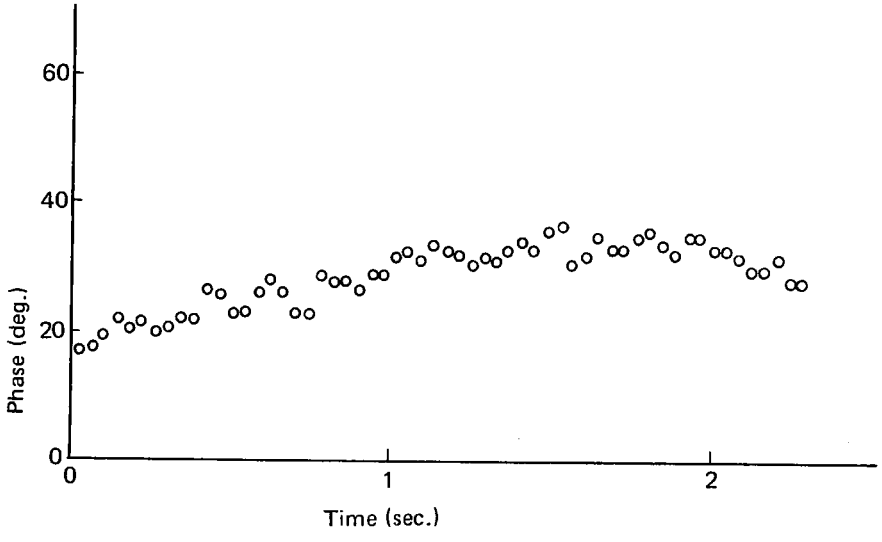

Fig. 3-5 Phase variation obtained by receiving CS.

Assuming that the propagation path through the atmosphere, especially troposphere, is approximately proportional to 1/sin (El), the path length at El of 1.7 deg. is about 25 times as long as that at El = 47.8 deg. On the other hand, the phase scintillation is directly proportional to propagation path length[24],[25],[26]. Therefore, the difference between phase variations of the signals from CS and INTELSAT can be regarded as that between the atmospheric phase scintillations, and then the phase variations of both signals from CS and INTELSAT can be regarded as the atmospheric phase scintillations. The phase variations due to the frequency standards and the equipments, superimposed in the phase variations of both signals, are removed, because we can assume the phase variations caused by the frequency standards and the equipments not to change statistically for the observation period (about a few tens minutes). The difference should be calculated in terms of the Allan variance, because the Allan variance of the signal including some power-law spectra is expressed by the series of the Allan variances corresponding to each spectrum[27]. The Allan variance is defined by

$$\sigma_\phi^2(k) = \frac{1}{N}\left\{\sum_{k=1}^{N} (\overline{\phi}_{k+1} - \overline{\phi}_k)^2/2\right\} \quad \cdots\cdots\cdots\cdots\cdots\cdots\cdots\cdots \quad (3.4)$$

where k is the time interval between the kth and the (k + 1)th samples. The Allan variance is related with the power spectral density. If the power spectral density P (ν) has the form

$$P(\nu) = C \cdot \nu^{\alpha} \quad \cdots\cdots\cdots\cdots\cdots\cdots\cdots\cdots\cdots\cdots\cdots\cdots\cdots\cdots \quad (3.5)$$

the corresponding Allan variance is

$$\sigma_{\phi}^{2}(k) = C' \cdot k^{-\alpha-1} \quad \cdots\cdots\cdots\cdots\cdots\cdots\cdots\cdots\cdots\cdots\cdots\cdots\cdots\cdots \quad (3.6)$$

where C and C′ are constants, and ν is a Fourier frequency of the variation of ϕ. Fig. 3-6 shows the Allan variance of the signals from CS and Fig. 3-7 shows the square root of the difference of the Allan variances of the signals from CS and INTELSAT. Fig. 3-7 indicates that the square root of the difference $\triangle\sigma_{\phi}$ obeys the 0.7～1.4th power law of averaging time T. This power law is equivalent to the power spectral density $P(\nu) \propto \nu^{-2.4 \sim -2.8}$, that is well coincident with the results of the phase scintillations obtained through the path on the ground.

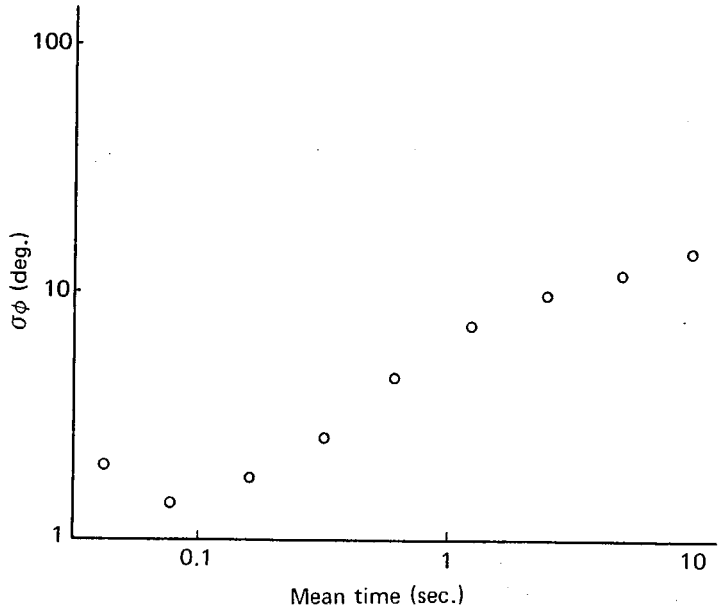

Fig. 3-6 Square root of the Allan variance for the phase variation of the signal from CS.

Assuming that the phase scintillations are directly proportional to path length, we can estimate the atmospheric phase scintillation at the zenith from the result at El = 1.7 deg., that is

$$\triangle\sigma_{\phi} \sim 0.2 \times T^{0.9} / \sqrt{\sin(El)} \quad \cdots\cdots\cdots\cdots\cdots\cdots\cdots\cdots\cdots\cdots\cdots\cdots \quad (3.7)$$

We usually observe radio stars at the higher elevation angle than 30 deg. Therefore, the phase scintillation at El = 30 deg. may be one of the fundamental values. The phase scintillation $\triangle\sigma_{\phi}$ at El = 30 deg. may exceed one radian when averaging time is 300 sec. or more, and

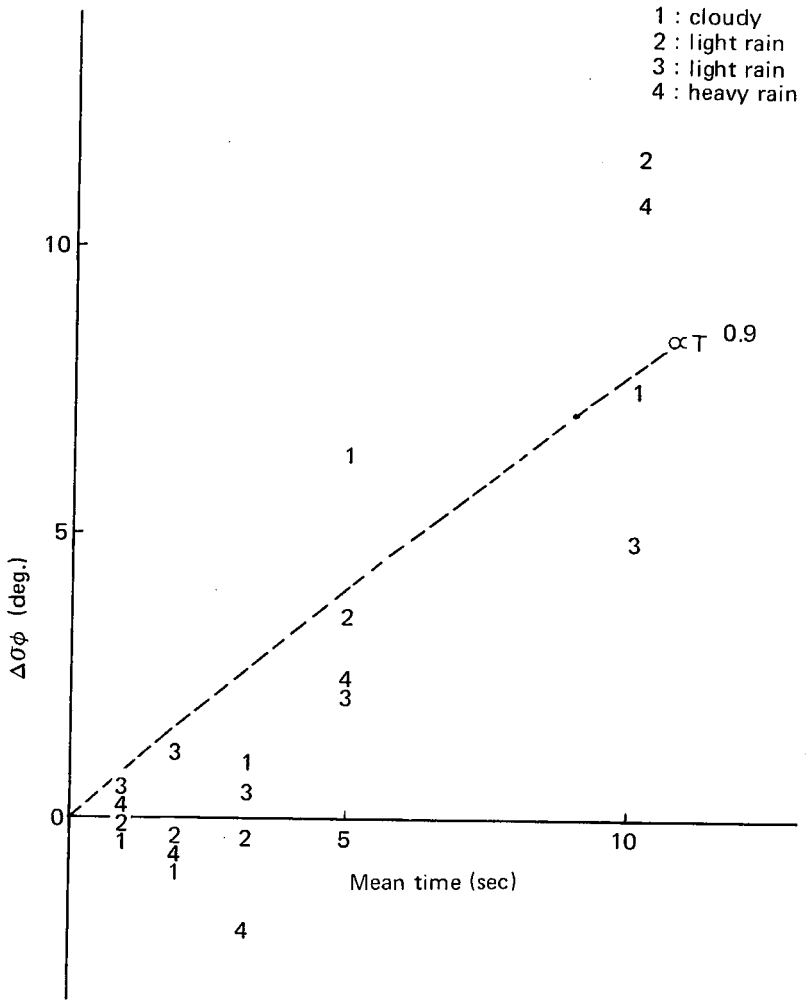

Fig. 3-7 Square root of the Allan variance of phase scintillations, $\Delta\sigma\phi$; square root of the difference of the Allan variances derived from the phase variations of the signals from INTELSAT and CS.

hence the coherence may decrease in such cases.

From Equation (1.66) the limitation of integration time mentioned above leads to the limitation of antenna diameter. In the common case that the estimation error of a phase and efficiency of an antenna are 0.1 radian and 0.5 respectively, and bandwidth and source flux density are 2 MHz and 1 J_y respectively, the product of two antenna diameters in VLBI system should be more than 76 m^2 for application to geodesy, astrometry or other fields in Japan, even if an H-maser frequency standards and a low noise amplifier are used. For example, if the main station adopts a 26 m antenna, the other station should have an antenna greater than 3 m.

Although the observations were carried out under the various meteorological conditions such as cloudy, light rain and heavy rain, the effects of rain or other precipitation were not defined from these observations.

4.5 Measurements of visibility scintillation due to the solar wind

Visibility scintillations are given by temporal variations of $|S_{xy}(\omega)|$ in Equation (1.20), and hence the observations of the visibility scintillation need not use the bandwidth synthesis. The observations were carried out from Sept. 18 to Oct. 14, 1980, receiving radio waves from QSO 3C273, Seyfert galaxy 3C84 and elliptical galaxy 3C279 with one channel. 3C84 and 3C279 were observed as calibration sources. 3C84 was at a long distance from the sun for the observation period, so it was not affected by the solar wind. 3C279, on the other hand, approached the sun and was occulted on Oct. 8. Especially, the radio flux intensity of 3C279 was too weak to measure the vibility scintillations. Furthermore, it was so close

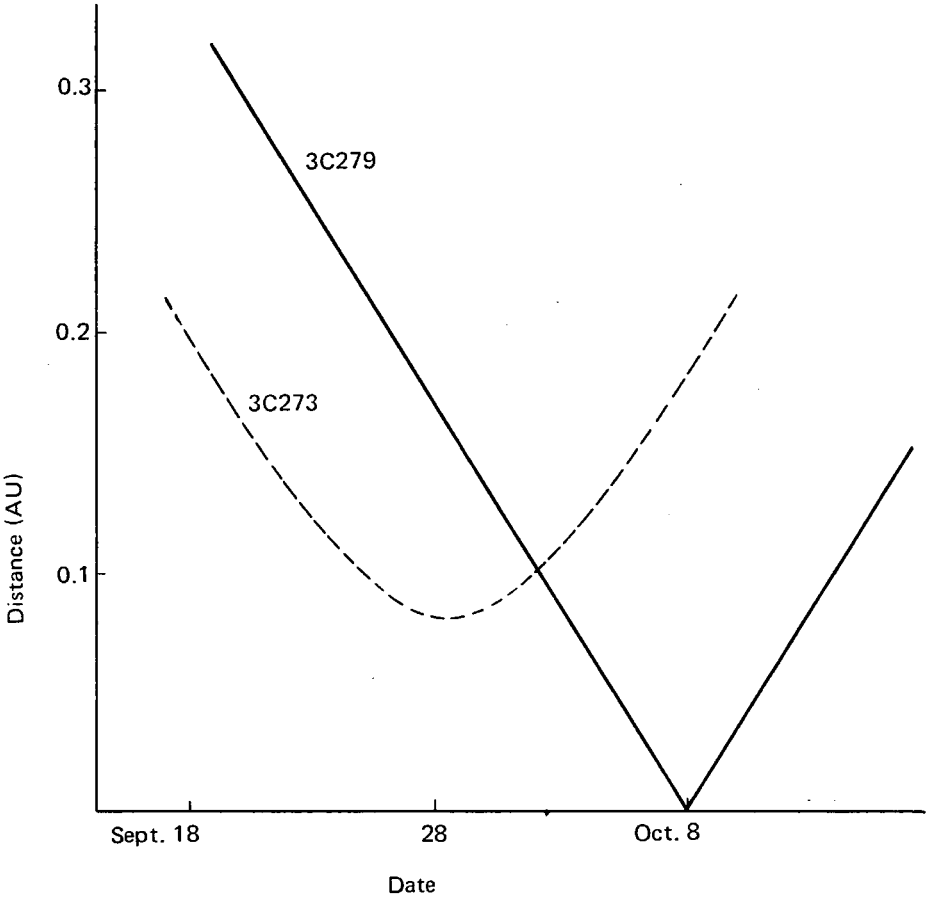

Fig. 3-8 Change of the distance between the propagation path from the radio source and the sun.

to the sun that the side-lobes of the antenna received undesired radio waves from the sun, and hence a signal-to-noise ratio rapidly decreased from Oct. 5 to Oct. 10. Consequently, only the data of 3C273 was available for the visibility scintillations.

Fig. 3-8 shows the change of the distance between the propagation path from the radio source and the sun. Fig. 3-9(a) shows the mean coherence (mean visibility) of the three

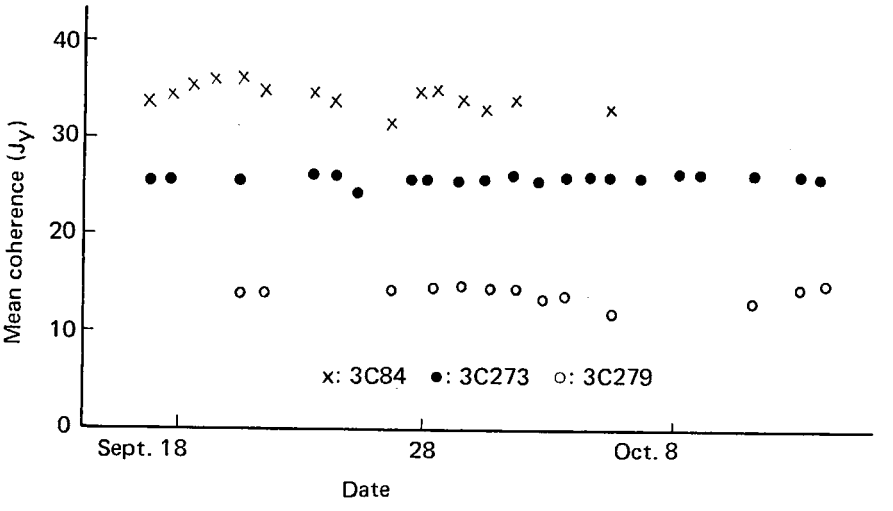

Fig. 3-9 (a) Mean coherence (visibility) of the three radio sources.

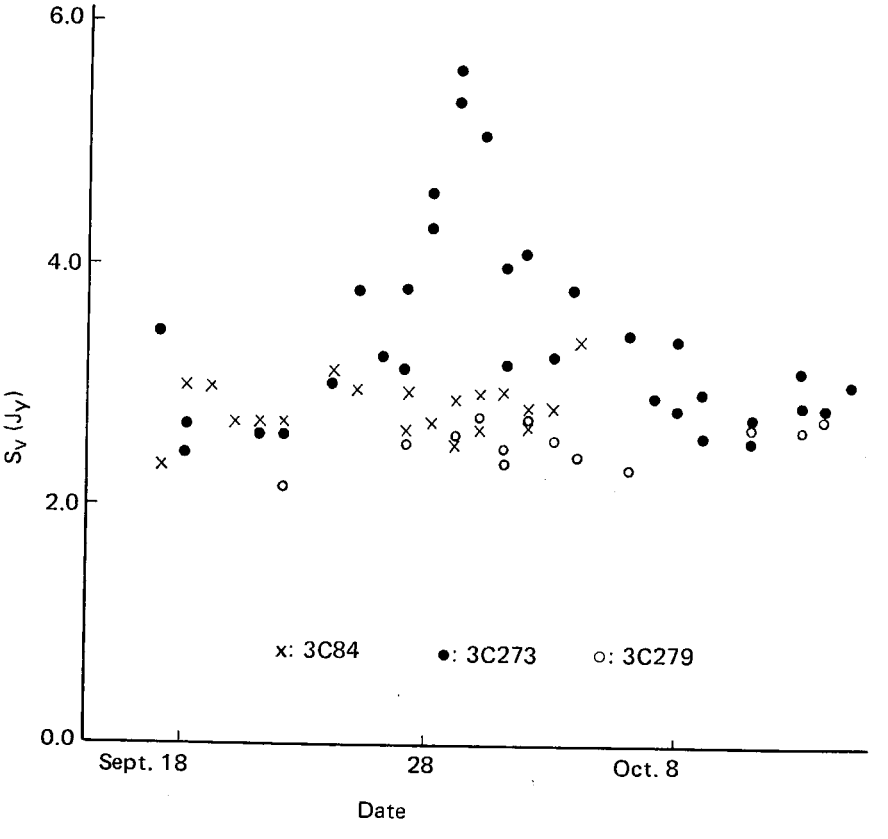

Fig. 3-9 (b) Visibility scintillation S_V due to the solar wind.

radio sources. The scattering of the mean visibility of 3C84 may be caused by its source structure, and the decrease for 3C279 on Oct. 6 and Oct. 11 is due to the undesired radio waves from the sun, mentioned above. On the other hand, the mean visibility of 3C273 is almost constant during the observation period.

Fig. 3-9(b) shows the visibility scintillation S_V in unit of J_y. The visibility scintillations S_V can be defined by

$$S_V = \left[\sum_{n=1}^{N} \left\{ |S_{xy,n}| - \left(\sum_{n=1}^{N} |S_{xy,n}| \right)/N \right\}^2 /N \right]^{1/2} \quad \cdots\cdots\cdots\cdots \quad (3.8)$$

where N is the number of measurements. The visibility scintillations of the signals from 3C273 rapidly increased when the propagation path approached the sun. When the distance was the nearest of 0.08 AU, it reached 10% of the total flux, above variations of about 3 J_y due to system noises. Fig. 3-10 shows the Allan variances of the visibility scintillations of

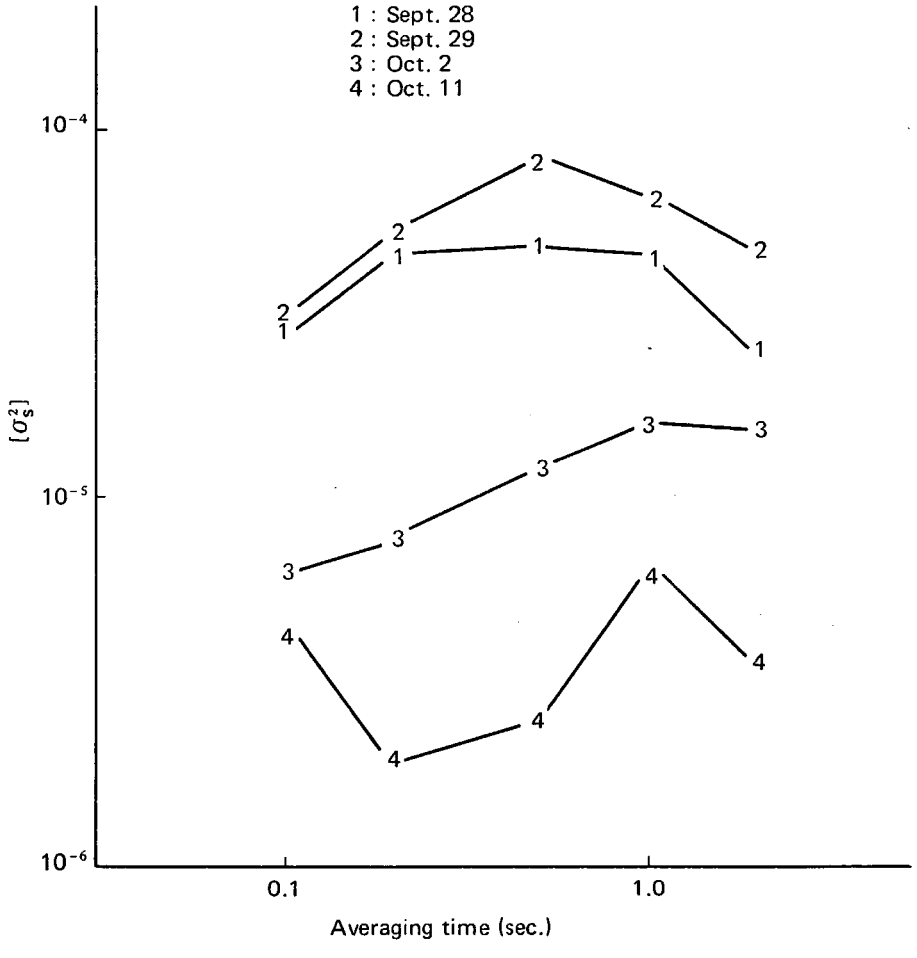

Fig. 3-10 Allan variances of the visibility scintillations for 3C273. $[\sigma_s^2]$ denotes the normalized σ_s^2 by the mean coherence.

3C273. The Allan variance σ_S^2 becomes maximum at mean time of $0.5 \sim 1.0$ sec. According to a theoretical investigation, the frequency range of the visibility scintillation observable with VLBI is limited to the frequency more than a baseline frequency ν_σ given by Cronyn[28]. In our VLBI system, the baseline frequency corresponds to 2 Hz, assuming the solar wind velocity estimated from Parker's model[29], [30]. The reciprocal of the estimated baseline frequency of 2 Hz is coincident with the observed value of $0.5 \sim 1.0$ sec.

Fig. 3-11 shows the visibility scintillation versus the distance between the paths from 3C273 and the sun. The visibility scintillation obeys approximately the 3rd power law of the distance. This result indicate that the Allan variance may become less than 10^{-5} rad^2 at integration time of 0.5 sec. and when the solar elongation exceeds $5 \sim 7$ deg., and hence the effect of interplanetary scintillations at 4 GHz may almost disappear over all scintillation frequencies for the VLBI system with a baseline of several tens km.

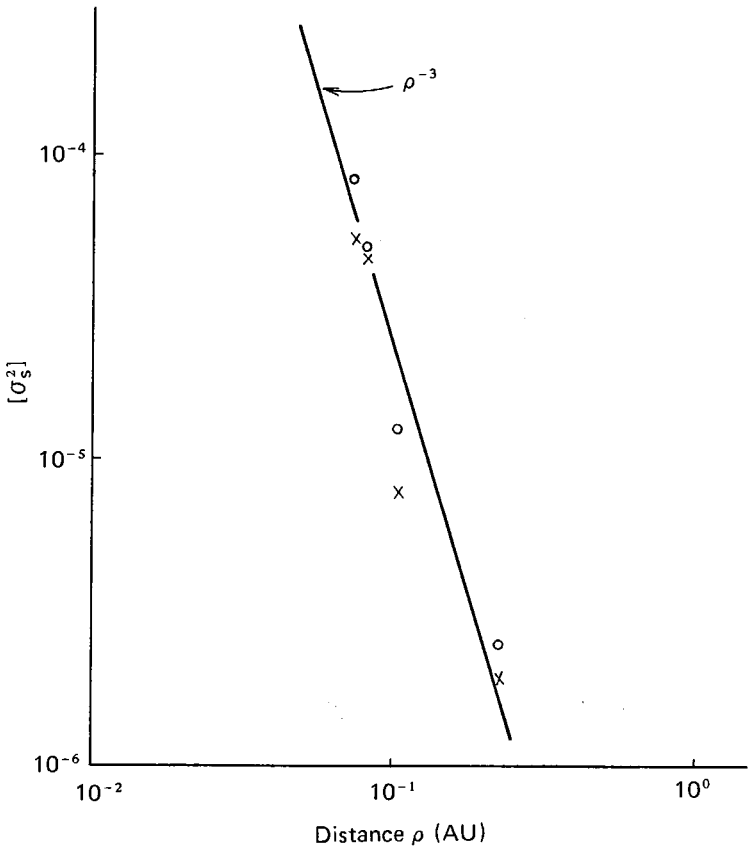

Fig. 3-11 Normalized visibility scintillation versus the distnace between the path from 3C273 and the sun.

Concluding Remarks

Accurate real-time VLBI system connected by a terrestrial microwave link was developed. This system adopts "minimum redundant bandwith synthesis", based on the linear

array theory and "multi-level fringe stopping in time domain" to make possible the precise determination of delay time and the measurement of short-term phase scintillations. The mini-computer (NEAC-3200) controls this total VLBI system and also has the functions of accurate program tracking and collection of the data from VLBI equipments.

The following remarks are concluded from the experiments using the accurate real-time VLBI system.

(1) The measurements of delay time were carried out by receiving synchronous satellite CS (Communications Satellite) and QSO 3C273. In the case of CS, the delay time was determined every 100 ms during which the integration time in each channel is equal to 20 ms by the method of the bandwidth synthesis. The estimation error of the delay time was about 0.1 ns. For the 20 consecutive data of the delay time, the peak-to-peak error and the r.m.s. error were 0.27 ns and 0.08 ns respectively. These results indicate that the delay time measurement accuracy in our system is about 0.1 ns, which corresponds to 3 cm in terms of optical path length. The slow variation of 0.02 ns/sec., which was the clock synchronization error caused by the frequency standards, superimposed on these data. On the other hand, in the case of QSO 3C273, the delay time was estimated every 10 sec., and then five consecutive data were obtained for 50 sec. The estimation error of delay time was 0.17 ns, by reason of insufficient integration time, and the clock synchronization error mentioned above made the large difference between the observational value and the calculated one (O-C). Thus, an H-maser frequency standard with frequency stability higher than 10^{-14} is required to observe a weak radio source with VLBI system.

(2) The phase differences at 4 GHz were obtained every 20 ms or 40 ms, receiving the radio waves from CS with one channel. The estimation error was 3～4 deg. The time variations of the phase difference also include the phase scintillations produced in the atmosphere and phase jitters due to the frequency standards. It can be assumed that these two variations are less than one deg. within the period of 0.5 sec. Therefore, the peak-to-peak error and the r.m.s. error were determined during the 0.5 sec. to estimate the error due to the instruments and data processing. These are 8 and 3 deg. respectively. From these results, the phase difference measurement accuracy is about 3 deg. and this value is approximately coincident with the phase error which gives the delay time error of 0.1 ns by the method of the bandwidth synthesis with 100 MHz span.

(3) The phase scintillations along the path through the atmosphere were observed for the first time using the real-time VLBI system. They were derived from the difference between the phase variations of the signals from two satellites, one at a rather high elevation and the other at a low elevation. The square root of the Allan variance of the phase scintillation, $\Delta\sigma_\phi$, obeys approximately $0.2 \cdot T^{0.7 \sim 1.4}$ deg. at the zenith, where T denotes the averaging time in sec. This function $^{\triangle}\sigma_\phi$, corresponds to the power spectral density $S(\nu) \propto \nu^{-2.4 \sim -2.8}$, which is the results obtained through the path on the ground. Although the observations were carried out under the various meteorological conditions such as are cloudy, of light rain and heavy rain, the effect of rain or other precipitation were not detected from these measurements. These results lead to the fact that $^{\triangle}\sigma_\phi$ at El = 30 deg. may exceeds one radian, and hence the coherence may decrease when the mean time or integration time becomes 300 sec. or more. This estimation suggests that the product of two antenna diameters in VLBI system should be more than 76 m^2 when the VLBI system is applied to geodesy, astrometry or other fields in Japan, even if an H-maser frequency standard and a low noise amplifier are used. For example, if the main station has a 26 m antenna, the other

station should have the antenna greater than 3 m.

(4) Phase scintillations due to the solar wind covering a wide frequency range $10^{-4} \sim 10^{-1}$ Hz were measured with a coherent dual frequency radio system on Mariner 10 by Woo et al. The phase scintillations were also measured using the VLBI system with the baseline of more than 1000 km by Knight et al. Both results show that the power spectrum density of the phase scintillations obeys the power law of frequency. On the other hand, we observed the visibility scintillations due to the solar wind in a rather short baseline.

The observations of the visibility scintillation due to the solar wind were carried out by receiving QSO 3C273 from Sept. 18 to Oct. 14, 1980. The visibility scintillations increased when the wave propagation path from QSO 3C273 approached the sun, and they reached 10% of the total flux, higher than the normal level, when the distance between the path and the sun was the nearest of 0.08 AU. The Allan variance of the visibility, σ_S^2, became maximum in the averaging time of $0.5 \sim 1.0$ sec. According to a theoretical investigation, the frequency range of the scintillations observed by a VLBI system is limited to the frequency higher than the baseline frequency given by Cronyn, so that the mean time 0.5 sec obtained by our observations is coincident with the reciprocal of the baseline frequency ν_σ estimated from the Parker's solar wind model. Furthermore, the visibility scintillations obey approximately the 3rd power law of the distance. These results show that $\sigma_S{}^2$ becomes less than 10^{-5} when the solar elongation exceeds $5 \sim 7$ deg., and hence the effect of the interplanetary scintillations at 4 GHz diminishes over all scintillation frequencies.

The results mentioned above show that our real-time VLBI system is superior to the first VLBI system in Japan (K-1), and has the same measurement accuracy as that of Mark III system with magnetic data recorders. The development of the Mark III system in USA is almost accomplished, and the system is all ready to use for the wide application fields such as geodesy, astrometry and radio astronomy. The Mark III system has a delay calibrator to calibrate the instrumental delay time, and also uses H-maser frequency standards so that it makes a long term integration in VLBI measurements possible.

Based on these achievements conducted with K-1 and K-2 systems, we have been developing K-3 VLBI system compatible with the Mark III system of USA. Although the accuracy of the K-3 system is same as that of the real-time VLBI system K-2, it includes H-maser frequency standards, a delay calibrator, and a water vapor radio-meter. On the other hand, a cooperative project agreement was made between NASA and RRL, and using K-3 and Mark III systems Japan-US joint VLBI experiment will start in early 1984 to measure global-scale plate motion, time synchronization error, polar motion, earth rotation, etc.

Acknowledgements

The wrok reported in this paper has made possible only through the cooperation and support of many people.

I am greatly indebted to Prof. M. Hirono, who provided constant support and expertise. Many people have been sources of encouragement and helpful technical discussions. Among them are Dr. K. Ikushima, Mr. N. Kawaguchi and Mr. F. Yamashita.

The development and experiment reported here were conducted by an item of ECS (Experimental Communications Satellite) project. I wish to express my cordial gratitutde to Dr. T. Ishida, Dr. N. Fugono, Dr. K. Yoshimura, Mr. R. Hayashi and the staffs of the ECS project.

I am also indebted to Dr. Y. Saburi and Mr. M. Kobayashi who provided constant support to the development of VLBI system.

References

(1) Rogers A. E. E., Radio Science, **5**, 10, 1239, Oct. 1970.
(2) Kawano N., Takahashi, F., Yoshino, T., and Kawajiri, N., IEEE/AP-S Digest 1980, **1**, 69, 1980.
(3) Kawaguchi, N. and Kawano, N., Review of Radio Res. Labs., **24**, 130, 539, Sept. 1978.
(4) Kawano N., Review of Radio Res. Labs. **24**, 130, 550, Sept. 1978.
(5) Thompson, M. C. and Vetter, M. J., Rev. Sci. Instr., **29**, 148, 1958.
(6) Herbstreit, J. W. and Thompson, M. C., Proc. IRE, 1391, 1955.
(7) Deam, A. P. and Fannin, B. M., Proc. IRE, 1402, 1955.
(8) Thompson, M. C., Wood, L. E., Janes, H. B. and Smith, D., IEEE, **AP-23**, 6, Nov. 1975.
(9) Baars, J. W. M. and Va, W., IEEE, **AP-15**, July, 1967.
(10) Basart, J. P., Miley, G. K. and Clark, B. G., IEEE, **AP-18**, 3, May, 1970.
(11) Hamaker, J. P., Radio Science, **13**, 5, 873, 1978.
(12) Woo, R., Yang, F. and Yip, K. W., Ap. J., **210**, 568, 1976.
(13) Knight, C. A., Robertson, D. S., Shaprio, I. I., Whitney, A. R., Rogers, A. E. E., Clark, T. A., Marandino, G. E., Vandenberg, N. R. and Goldstein, R. M., Bull. AAS, 3, 447, 1971.
(14) Whitney, A. R., Ph. D. Thesis, MIT, 1974.
(15) Whitney, A. R., Rogers, A. E. E., Hinteregger, H. F., Knight, C. A., Levine, J. I. and Lippincott, S., Radio Science, **11**, 5, 421, May, 1976.
(16) Kawano, N., Review of Radio Res. Labs., **24**, 130, 455, 1978.
(17) Thomas, J. B., NASA Technical Report, 32-1526, VIII, 28, 1972.
(18) Van Vleck, J. H. and Middleton, D., Proc. IEEE, **54**, 1, 2, 1966.
(19) Moffet, A. T., IEEE, **AP-16**, 2, 172, March, 1968.
(20) Robertson, D. S., Ph. D. Thesis, MIT, 1975.
(21) Rice, S. O., BSTJ, **23**, 282, July 1944.
(22) Matsumoto, K., Review of Radio Res. Labs. **26**, 137, March 1980.
(23) Fujita, M., Review of Radio Res. Labs. **25**, 135, Dec., 1979.
(24) Tatarski, V. I., "Wave Propagation in a Turbulent Medium", MacGraw-Hill, 1961.
(25) Muchmore, R. B. and Wheelon, A. D., Proc. IRE, 1437, Oct. 1955.
(26) Wheelon, A. D. and Muchmore, R. B., Proc. IRE, 1450, Oct. 1955.
(27) Yoshimura, K., IEE Japan Technical Report, (II) 41, 17, 1976.
(28) Cronyn, W. M., Ap. J., **174**, 181, May 1972.
(29) Cohen, M. H. and Gundermann, E. J., Ap. J., **155**, Feb. 1969.
(30) Parker, E. J., Space Sci. Rev., **4**, 666, 1965.